BIOCHEMISTRY
including biophysical chemistry & molecular biology

Article

pubs.acs.org/biochemistry

Evidence for Substrate Binding-Induced Zwitterion Formation in the Catalytic Cys-His Dyad of the SARS-CoV Main Protease

Alexander Paasche,[†] Andreas Zipper,[†] Simon Schäfer,[†] John Ziebuhr,[‡] Tanja Schirmeister,[§] and Bernd Engels*[,†]

[†]Institut für Physikalische und Theoretische Chemie, Universität Würzburg, Emil-Fischer-Straße 42, 97074 Würzburg, Germany
[‡]Institut für Medizinische Virologie, Justus-Liebig-Universität Gießen, BFS, Schubertstraße 81, 35392 Gießen, Germany
[§]Institut für Pharmazie und Biochemie, Johannes Gutenberg-Universität Mainz, Staudinger Weg 5, 55128 Mainz, Germany

Supporting Information

ABSTRACT: The coronavirus main protease (M^{pro}) represents an attractive drug target for antiviral therapy of coronavirus (CoV) infections, including severe acute respiratory syndrome (SARS). The SARS-CoV M^{pro} and related CoV proteases have several distinct features, such as an uncharged Cys-His catalytic dyad embedded in a chymotrypsin-like protease fold, that clearly separate these enzymes from archetypical cysteine proteases. To further characterize the catalytic system of CoV main proteases and to obtain information about improved inhibitors, we performed comprehensive simulations of the proton-transfer reactions in the SARS-CoV M^{pro} active site that lead to the Cys^-/His^+ zwitterionic state required for efficient proteolytic activity. Our simulations, comprising the free enzyme as well as substrate−enzyme and inhibitor−enzyme complexes, lead us to predict that zwitterion formation is fostered by substrate binding but not inhibitor binding. This indicates that M^{pro} employs a substrate-induced catalytic mechanism that further enhances its substrate specificity. Our computational data are in line with available experimental results, such as X-ray geometries, measured pK_a values, mutagenesis experiments, and the measured differences between the kinetic parameters of substrates and inhibitors. The data also provide an atomistic picture of the formerly postulated electrostatic trigger involved in SARS-CoV M^{pro} activity. Finally, they provide information on how a specific microenvironment may finely tune the activity of M^{pro} toward specific viral protein substrates, which is known to be required for efficient viral replication. Our simulations also indicate that the low inhibition potencies of known covalently interacting inhibitors may, at least in part, be attributed to insufficient fostering of the proton-transfer reaction. These findings suggest ways to achieve improved inhibitors.

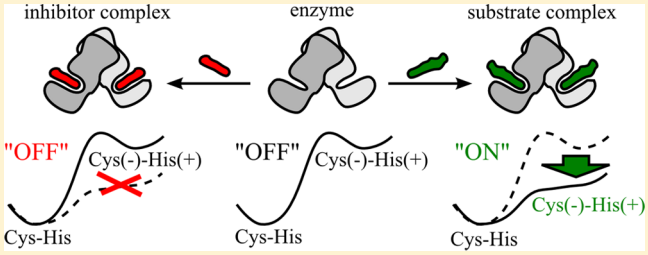

Over the past few years, the SARS coronavirus main protease (SARS-CoV M^{pro}) has been extensively studied, mainly because it is an interesting drug target for specific antiviral therapy of severe acute respiratory syndrome (SARS).[1−7] Furthermore, biochemical and structural studies of related CoV main proteases revealed the conservation of key residues involved in catalysis and substrate specificity,[2,5,6,8,9] making the SARS-CoV M^{pro} an excellent model for developing broad-spectrum inhibitors targeting a wide range of human and animal coronaviruses. The urgent need for developing such inhibitors became apparent by the global SARS epidemic which emerged in Southern China in 2002−2003 and rapidly spread worldwide, infecting a total of 8096 people and causing 774 deaths,[10] and this need is now reinforced by the identification of a novel human beta-coronavirus that recently emerged in the Middle East and, similar to SARS, appears to be associated with severe respiratory disease and high mortality.[11−14]

Irreversible inhibition involves the formation of a covalent bond between the electrophilic group of the inhibitor (warhead) and an active-site residue of the enzyme, thereby producing a dead-end complex. Hence, in such cases the inhibition potency partly depends on the reactivity of the electrophilic group. A survey of irreversible CoV M^{pro} inhibitors developed over the past 10 years (Table 1) reveals that none of the compounds exhibits a reaction constant k_i greater than 0.05 s^{-1}, which is considerably lower than the corresponding k_{cat} values of the substrate (0.8−3.3 s^{-1}).[15,16] The same also holds for some reversible inhibitors (Table 1) which are known to interact covalently with the enzyme. Such small k_i values are surprising, given that the same warheads were shown to react much more efficiently with other cysteine proteases.[17]

The active site of SARS-CoV M^{pro} displays several distinct features compared to archetypical cysteine proteases.[2,3] Experimental pK_a measurements further suggested that, in striking contrast to the thiolate/imidazolium ion pair found in papain[18−25] or cathepsins,[26] the SARS-CoV M^{pro} catalytic residues Cys145 and His41 adopt an uncharged resting state.[27]

Received: May 14, 2013
Revised: August 22, 2014
Published: August 25, 2014

   dx.doi.org/10.1021/bi400604t | *Biochemistry* 2014, 53, 5930−5946

Table 1. Overview of Previously Reported Irreversible Inhibitors of the SARS-CoV M^{pro} [a]

year	warhead	K_i	k_i (s^{-1})	IC_{50}	PDB	ref
2003	chloromethyl ketone			2 mM	1UK4	Yang et al.[3]
2005	α,β-unsaturated ester	6.7 μM	0.0022		2AMD	Yang et al.[5]
2005	α,β-unsaturated ester	0.52 μM				Shie et al.[127]
2005	α,β-unsaturated ester		0.0002	45 μM	2ALV	Ghosh et al.[101]
2005	etacrynic acid derivative	35.3 μM				Kaeppler et al.[128]
2005	epoxide	18 μM	0.035		2A5I	Lee et al.[102]
2005	aziridine					Martina et al.[129]
2006	benzotriazole ester	7.5 nM[b]	0.0011			Wu et al.[130]
2006	aldehyde	0.05 μM			2GX4	Yang et al.[98]
2007	epoxide				2GTB	Lee et al.[95]
2007	α,β-unsaturated ester	1.9 μM	0.035		2HOB	Xue et al.[96]
2007	α,β-epoxy ketone	2.2 μM	0.004		2OP9	Goetz et al.[103]
2007	phthalhydrazide	0.25 μM			2Z3C	Yin et al.[97]
2008	aldehyde			37 μM		Akaji et al.[131]
2008	benzotriazole ester	1.38 μM	0.013		2V6N	Verschueren et al.[99]
2011	α,β-unsaturated ester			330 μM	3AVZ	Akaji et al.[104]
2011	aldehyde	2.2 μM			2SN8	Zhu et al.[105]
2013	nitrile			4.6 μM	3VB3	Zhu et al.[100]

[a]The warhead describes the chemical moiety that was used as electrophilic building block to attain irreversible inhibition. Respective K_i, k_i, or IC_{50} values are given as published. Available X-ray structures of enzyme−inhibitor complexes are indicated by four-letter Protein Data Bank identifiers used by the Research Collaboratory for Structural Bioinformatics (RCSB).[34] [b]K_i values reported in this work could not be reproduced by Verschueren et al.,[99] who measured significantly reduced inhibition potency in the micromolar range. Please note that aldehyde-based[105,131] and nitrile-based[100] inhibitors, which are known to react covalently, are weak reversible inhibitors.

The well-known low reactivity of thiols compared to thiolates indicates that, prior to the actual chemical reaction between enzyme and substrate, the active site of the enzyme has to be activated. This might happen through a proton transfer, leading to a very reactive thiolate that represents the reactive species in many other proteolytic reactions. Furthermore, the determination of turnover rates of ester and amide substrates hydrolyzed by SARS-CoV M^{pro} revealed similar kinetic parameters under both steady-state and pre-steady-state conditions, although the chemical reactivities of the two substrates differ by a factor of 2000 in aqueous media in the absence of enzymatic activity.[15] These and other data suggested a proteolytic mechanism for CoV main proteases that, at least in part, differs from that employed by cellular cysteine proteases such as papain-like cathepsins. The specific catalytic properties of CoV main proteases might also explain the relatively poor success with developing highly active, covalently interacting inhibitors targeting these enzymes (Table 1). Previously performed model calculations of inhibition reactions of thiol-containing enzymes have indicated that the proton transfer leading to the thiolate/imidazolium ion pair is a necessary (and often rate-limiting) step in the inhibition reaction.[28] The limited success of the inhibitors summarized in Table 1 may be due to the fact that these inhibitors (in contrast to natural substrates) do not (or less efficiently) promote this proton transfer. The Lewis structures of selected inhibitors are illustrated in Table S1 of the Supporting Information.

To get further insight into the mechanisms involved in catalyzis and inhibition of the SARS-CoV M^{pro}, we decided to perform a detailed atomistic study. Using a range of theoretical approaches, we sought to develop a theoretical model that accommodates previous experimental findings, such as the existence of a neutral Cys-His catalytic dyad (rather than thiolate/imidazolium pair), and may be suitable to identify factors involved in the distinct catalytic mechanisms of the SARS-CoV M^{pro}. As a starting point for our computational studies, we used a range of X-ray structures available for SARS-CoV M^{pro}. Furthermore, we took advantage of structures reported previously for inhibitor and substrate complexes, which allowed us to evaluate possible effects arising from substrate or inhibitor binding.

The theoretical study was performed as follows. First, molecular dynamics (MD) simulations were conducted and compared to the available X-ray structures. This allowed us to identify the most likely protonation state of the active-site residues. Second, on the basis of the identified protonation state, possible proton-transfer reactions within the active site were evaluated in order to identify possible charge-relay mechanisms. Because the latter would involve bond breakages, quantum mechanics/molecular mechanics (QM/MM) calculations were employed in these analyses. Third, to obtain insight into factors that might promote or inhibit ion pair formation, the electrostatic contributions around the active site sphere were investigated using charge deletion analysis (CDA). In a final step, free energy calculations, based on QM/MM/MD simulations, were conducted to obtain thermodynamic and kinetic information on the proton-transfer reaction between cysteine and histidine, including specific entropic contributions. Conclusions derived from these theoretical studies regarding potential functional roles of specific residues in the M^{pro} active site were supported by the CoV-wide conservation (or conservative replacements) of these residues. Taken together, the data provide a basis for future studies into the inhibition reaction occurring at the active site of the SARS-CoV M^{pro} and are expected to facilitate the development of more-effective inhibitors.

MATERIALS AND METHODS

Comparative Molecular Dynamics Simulations. All MD simulations were conducted with the NAMD 2.6 parallel molecular dynamics software.[29,30] Each of the six simulations contained an overall number of about 68 500 atoms and was simulated for 10 ns by using time steps of 1 ps. Solvent was

dx.doi.org/10.1021/bi400604t | Biochemistry 2014, 53, 5930−5946

explicitly included in the simulations as a droplet approach and comprised a diameter of 110 Å for the employed water shell. Simulations were conducted as NVT ensemble, by using the Verlet integration method[31] and the SHAKE algorithm[32] for the water molecules to reduce internal degrees of freedom. Furthermore, constraints were applied by using a spherical boundary condition beyond a radius of 55 Å from the model system's center of mass, to prevent water molecules from evaporating from the solvent shell into vacuum during the simulation.

All simulations were based on the PDB structure 2DUC[33] of the SARS-CoV M^{pro} dimer that was obtained from the RCSB database.[34] They were performed in an identical manner using the following protocol. The protonation state of titratable residues, such as histidines, were set according to a pH value of 7, and empirical pK_a value predictions were made using the PROPKA methodology.[35−37] The protonation states of the active-site residues His41, Cys145, and the neighboring His164 residue were set according to one of the six possible protonation states, as shown in Scheme 2 in the Results and Discussion, in six individual MD simulations. The protein structures were embedded in a TIP3 water shell[38] and water molecules initially minimized in their energy for 1000 steps to remove molecular strains, especially at the protein−water interface. Subsequently, the model systems were heated in gradual steps of 10 K until reaching the final simulation temperature of 310 K, while keeping the protein structure fixed. After heating, simulations were equilibrated for 1 ns under successive release of the spatial constraints that were put on the protein backbone. Finally, production runs were performed for 10 ns and trajectories recorded in 10 000 step windows, resulting in 1000 frames for each simulation. Subsequent data analysis for root-mean-square deviation (RMSD) plotting and statistical structure analysis (histograms) were performed with VMD.[39] The respective RMSD values as a function of simulation time are given in the Supporting Information.

Histogram analysis for the Cys145−His41 distance was based on atom distances between sulfur (Cys145) and nitrogen (His41) for each trajectory. A binning size of 0.05 Å was employed for the distance range from 2.0 to 10.0 Å and the number of counts per bin were taken relative to the overall number of 1000 recorded distances.

QM/MM Potentials. QM/MM potential energy surfaces (PESs) were calculated with the Chemshell 3.2 software package.[40] The QM/MM system was set up from a representative snapshot of the MD simulation according to the **Cys145-His41-His164** state. The water shell was reduced to a radius of 30 Å around the active-site residues and further kept fix for radii greater than 10 Å to save computational resources during energy minimizations. Water molecules within the radius of 10 Å were kept rigid with respect to internal degrees of freedom, with the exception of the bridging water molecules involved in proton-transfer reactions. The employed QM part was defined by the side chains of active-site residues Cys145 and His41, His164, and the two bridging water molecules as shown in Figure 2 and further illustrated in Figure 3 in the Results and Discussion. Calculations of the QM part were performed with the TURBOMOLE 5.9 suite of programs.[41] High-level approaches which are needed for some properties or special reactions[42,43] are too expensive for the present study. Because a recent benchmark study[44] proved the good ratio between accuracy and computational costs, the B3LYP exchange correlation functional[45−47] in combination with a TZVP basis set[48,49] was used for energy calculations "on top" of the RI-BLYP/TZVP structure optimizations,[45,49−53] as successfully applied in several earlier studies.[26,28,54−57] According to a recent benchmarking,[44] the error with respect to structure optimizations on the B3LYP/TZVP or even higher level of theory can be expected to be below 2 kJ/mol. The benchmark also showed that in comparison to the LCCSD(T)/QZVP method the present approach underestimates the energy difference between the neutral and zwitterionic state by about 17 kJ/mol. For the MM part, the CHARMM22 all-atom force field[58] was employed. For QM/MM coupling and boundary treatment across chemical bonds, an electrostatic embedding scheme[59] and furthermore the link atom approach[60] were employed. Detailed reviews of the applied approaches have been published previously by Senn and Thiel,[61] and others.[62,63]

Valid reaction coordinates that connect the different protonation states between the active-site residues Cys145, His41, and His164 in a meaningful way were carefully identified by probing multiple PES calculations with different combinations of bond length changes within the complex hydrogen bond network, as shown in the Results and Discussion in Figure 2. The reaction coordinates r_1(O−H) and r(N−H) were assessed to be suitable descriptors to model the proton-transfer reactions between Cys145/His41 and His41/His164. Relaxed QM/MM PESs were mapped by changing the reaction coordinates in incremental steps of 0.1 Å and subsequent constrained energy minimizations with respect to the two coordinates for each grid point. For energy minimizations, hybrid delocalized internal coordinates (HDLC)[64] were used.

Averaged QM/MM energy potentials for the proton transfer between the **Cys145-His41-His164** and **Cys145(−)-His41(+)-His164** states were calculated for three QM/MM setups that were prepared using the procedure described above for the QM/MM energy surfaces. The three model systems (free enzyme, inhibitor-bound enzyme, and substrate-bound enzyme) were based on X-ray structures 2DUC,[33] 2AMD,[5] and 2Q6G,[6] as illustrated in the Results and Discussion in Figure 3. For the averaging of proton-transfer potentials, 10 snapshots were taken from each MD simulation, one for each 1 ns window over the whole simulation time of 10 ns. The QM part was restricted to the relevant parts, comprising the side chains of the Cys145 and His41 residues, and also included one bridging water molecule in the case of the free enzyme. QM/MM energy curves were calculated in forward and backward directions to ensure meaningful minimum energy paths for the transition between the **Cys145-His41-His164** and **Cys145(−)-His41(+)-His164** states. Therefore, averaging was done in sum over 20 minimum energy paths that were aligned by least-squares fitting technique. Furthermore, standard deviations for the relative energies ΔU were calculated for each point of the proton-transfer curve.

Charge Deletion Analysis. The CDA, also denoted as decomposition analysis, computes changes in the relative energies $\Delta\Delta U$ that are due to switching off the electrostatic point charges for certain parts of the QM/MM system by simply setting them to zero. This method has been applied successfully in different forms by several other QM/MM studies.[26,65−69] For the given purpose, the two minima **Cys145-His41-His164** and **Cys145(−)-His41(+)-His164** that are located at r(S−H) = 1.4 Å and r(S−H) = 2.0 Å were taken from the 11 calculated proton-transfer potentials, as described above, and calculated for their relative QM/MM energy. This difference between the neutral (N) and zwitterionic state (ZW) is abbreviated ΔU(ZW). Then, a series of QM/MM energy calculations were repeated with

dx.doi.org/10.1021/bi400604t | Biochemistry 2014, 53, 5930−5946

identical structures, but with individual residues that were deleted by their point charges in the MM part. This was done for the side chains of each of the amino acids Arg40, His164, Phe181, and Asp187 and the whole salt bridge formed by the Arg40−Asp187 residues. Other important parts around the active site, like the buried water molecule H_2O@His41, the inhibitor, or the substrate, were also included in the analysis. Furthermore, the solvent water shell, the whole protein structure, and the individual protomers A and B were switched off, respectively. The difference between the obtained energy $\Delta U(\mathrm{ZW})^{\text{MM charges off}}$, when switching off a certain part of the system, and the unaffected relative energy $\Delta U(\mathrm{ZW})$ gives an estimate of the stabilizing or destabilizing electrostatic effect of this part on the **Cys145(−)-His41(+)-His164** state.

$$\Delta\Delta U(\mathrm{ZW}) = \Delta U(\mathrm{ZW})^{\text{MM charges off}} - \Delta U(\mathrm{ZW})$$

The sign of the ΔU values indicates whether the selected part has a stabilizing or destabilizing impact on the formation of the zwitterion. Positive energy values for ΔU indicate a stabilizing contribution, whereas negative values indicate a destabilizing effect. To take structural fluctuations during the MD into account,[70−75] averaging was done over 11 snapshots, similar to the procedure described for the proton-transfer potential. This also allowed the calculation of standard deviations in order to get an estimate for the fluctuation of the electrostatic contribution.

Free Energy Calculations. Free energy potentials of the cysteine histidine proton transfer were obtained by QM/MM potential of mean force (PMF) calculations,[76] using the AMBER 11 suite of programs.[77] Simulations were performed for the free enzyme and the substrate-bound model. Reasonable starting structures were already available from the classical MD simulations. The selection of the QM part was done as for the QM/MM minimum energy path calculations and included the side chains of Cys145 and His41, and one bridging water molecule in the case of the free enzyme. The semiempirical PM3/PDDG method[78,79] was employed for the quantum chemical calculations because it was recently proven by benchmarking data to be more reliable than other semiempirical Hamiltonians (RM1, AM1, MNDO).[44] Nevertheless, the benchmarking results have shown that PM3/PDDG overestimates the energy difference between the neutral and the zwitterionic state by about 21 kJ/mol (LCCSD(T)/QZVP benchmark). This means that in comparison to the B3LYP/TZVP methods which are used for the QM/MM minimum energy path calculation a difference of 38 kJ/mol can be expected. For the MM part, the ff99SB parameter set from Hornak and Simmerling[80] was employed, as implemented in AMBER. The two model systems were set up identically to the classical MD simulations, comprising spherical boundary conditions, 1 fs time steps, and 310 K simulation temperature. In order to perform PMF calculations, an umbrella sampling[81,82] was employed by using a bias potential along the reaction coordinate. Each window was simulated for 50 ps. The influence of the simulation length on the PMF results is shown in the Supporting Information which gives an estimate of the change in relative energies in relation to the sampling period applied. Although longer simulation time provided better results, the sampling times had to be restricted to 50 ps in order to keep computational costs at a reasonable level. Despite these slight limitations, the maximum deviation between relative energies obtained by 50 and 100 ps was consistently found to be below 16 kJ/mol and, thus, clearly below the intrinsic error of the PM3 Hamiltonian. The bias potential was set up for the r(S−H) bond of Cys145 and the r(N−H) distance of His41 in the case of the substrate-bound model system, as illustrated in Figure 3e in the Results and Discussion. The proton transfer required 16 simulation windows with incremental shifts of 0.1 Å for the bias potential minimum to achieve the transition from the **Cys145-His41-His164** to the **Cys145(−)-His41(+)-His164** state. For the free enzyme, which involves a water-mediated proton transfer, the calculation of a two-dimensional PMF energy surface with 272 simulation windows was necessary to obtain the minimum energy path that connects the **Cys145-His41-His164** and **Cys145(−)-His41(+)-His164** state. Here, the r(S−H)/r_1(O−H) and r_2(O−H)/r(N−H) coordinates were used, as illustrated in the next section in Figure 3d.

RESULTS AND DISCUSSION

Comparative Molecular Dynamic Simulations. A topological analysis of the SARS-CoV M^{pro} active site reveals an interesting network of amino acids that exhibit different possibilities for individual protonation states of the titratable residues. The active site of the SARS-CoV M^{pro} and its neighboring residues (Scheme 1) contains four titratable residues, Cys145, His41, His164, and Asp187, that, hypothetically, could exist in a variety of different protonation state combinations. Permutation of all these protonation states would formally lead to 2^4 (16) possible combinations. Asp187 forms a salt bridge with Arg40. It seems reasonable to suggest that this residue has an deprotonated carboxylate group, since protonation of the Asp187 COO^- moiety would lead to the disruption of the salt bridge which, in turn, would require to overcome a stabilizing energetic contribution of about 15 kJ/mol.[83] Furthermore, we considered it extremely unlikely that positive charges of residues His41 and His164 are positioned next to each other. The remaining six hypothetical combinations of protonation states for the residues Cys145, His41, and His164

Scheme 1. Schematic Drawing of the Catalytic Dyad Cys145/His41 of SARS-CoV M^{pro} and Selected Neighboring Residues Potentially Involved in Enzyme Catalyzis[a]

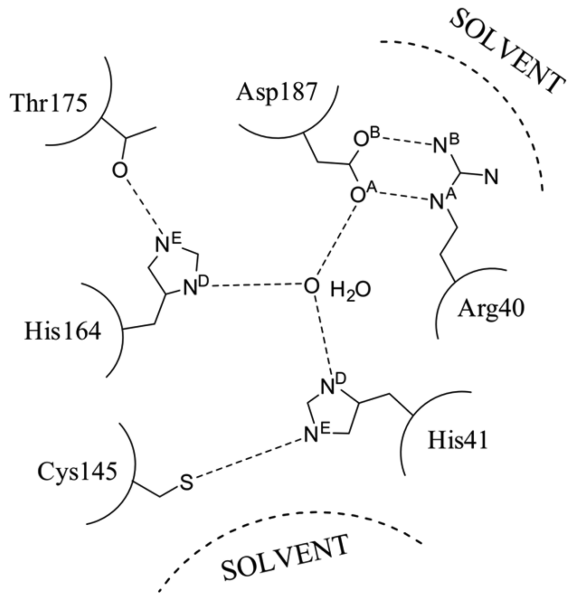

[a]Hydrogen atoms are omitted for the sake of clarity. The water molecule in the middle (H_2O@His41) possesses a stable position and is trapped between His41, His164, and Asp187.

dx.doi.org/10.1021/bi400604t | Biochemistry 2014, 53, 5930−5946

Scheme 2. Six Possible Protonation States of the Active-Site Residues Cys145, His41, and His164[a]

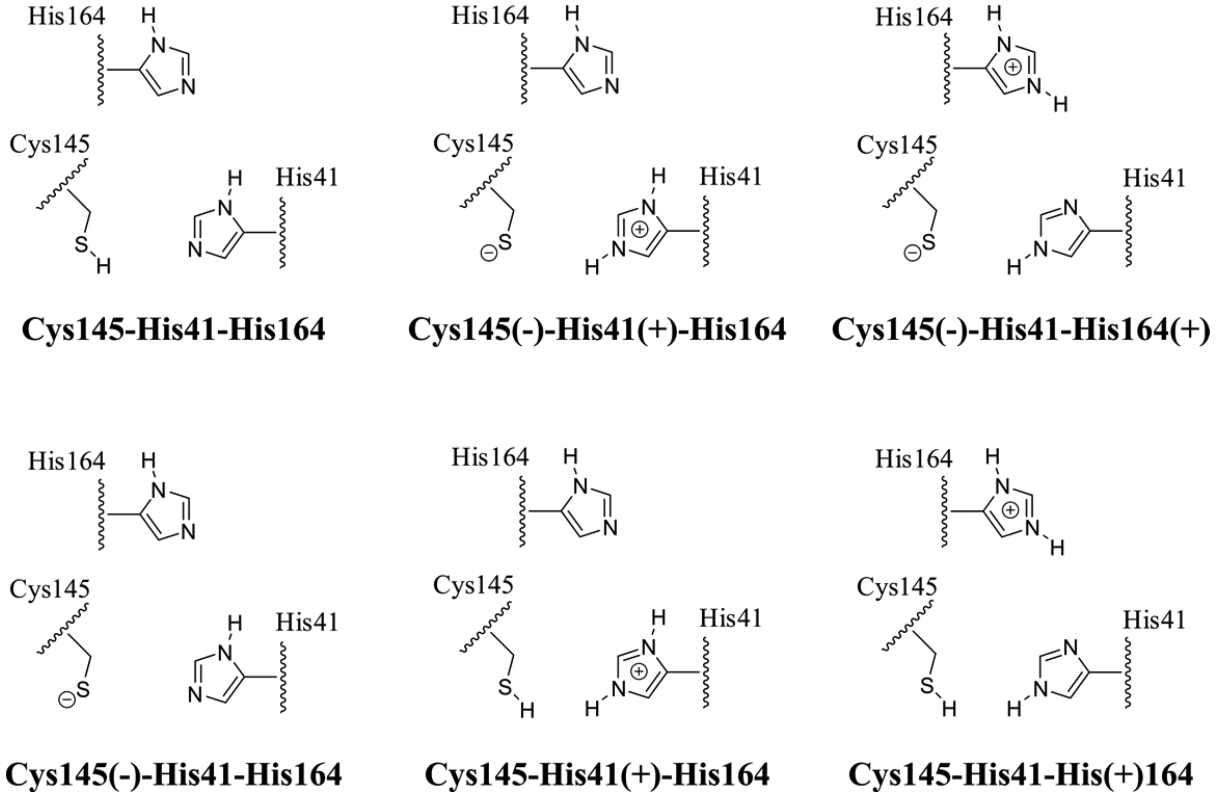

[a]Water molecules are neglected in this scheme for the sake of clarity. A complete scheme with the topology of the active site of SARS-CoV M^{pro} is given in Scheme 1.

are depicted in Scheme 2. Although some combinations appear more likely than others, it was not possible to draw definitive conclusions regarding the predominant situation.

Generally, X-ray structures do not provide direct information on the protonation states of specific residues because only heavy atoms are detectable using routinely applied procedures of X-ray crystallography. To some extent, however, information on protonation states may be derived from the structural arrangement of heavy atoms whose precise positions are affected by the underlying hydrogen bond networks. Hence, structural comparison of different theoretical protonation state models, such as those obtained by MD simulations, with the experimentally determined X-ray structure may help to identify (most) probable and less likely protonation states. A key parameter in this analysis is the degree of similarity between simulated and experimental structure which can be ranked using RMSD values or important geometric parameters.

In this study, we simulated six possible protonation states with identical work flows for 10 ns, as described in the theoretical calculations section, and analyzed their structural properties. The quality of the MD simulations was assessed by determining the RMSD of the frames with respect to the first frame of the simulation. Detailed plots of RMSD values are given as a function of simulation time in the Supporting Information. All simulations remained stable after a period of about 1 ns and possessed average RMSD values between 1.7 and 2.1 Å over the whole simulation time of 10 ns. Although minor differences were observed for the individual simulations they were considered too small to draw reliable conclusions.

The distance between the catalytic residues Cys145 and His41 may provide a more suitable criterion for comparisons as suggested previously in MD studies of the SARS-CoV M^{pro}.[84,85] A comparative histogram analysis of the observed Cys145−His41 distances recorded throughout the individual trajectories is shown in Figure 1. The histograms show the distance values that are most likely observed during the simulation, together with their statistical distribution along the distance axis. Furthermore, the distribution profiles were compared to the experimentally available Cys145−His41 distances from six published X-ray structures. The comparison of the individual histograms shows very broad distance distributions for the **Cys145(−)-His41(+)-His164** and **Cys145-His41(+)-His164** protonation states, slightly sharper distributions for the **Cys145(−)-His41-His164** and **Cys145-His41-His164(+)** configurations, and apparent sharp peaks for the distributions of the two protonation states **Cys145-His41-His164** and **Cys164(−)-His41-His164(+)**. Beside these narrow distance distributions, the latter ones also revealed the best agreement with the experimental values obtained by X-ray crystallography. The data lead us to conclude that **Cys145-His41-His164** and **Cys145(−)-His41-His164(+)** are the most probable proton configurations for the considered active-site residues. However, on the basis of these data it was not possible to infer which one of the two configurations is predominant, since the distance profiles obtained proved to be very similar.

To gain more detailed information, the comparison between the MD simulation results and the X-ray structures was extended by using a set of three additional geometry parameters that includes structure information on a slightly larger part of the active site. For this purpose, the hydrogen bond network involving His41 was considered more extensively, including the buried water molecule H_2O@His41 that occupies a position

dx.doi.org/10.1021/bi400604t | Biochemistry 2014, 53, 5930−5946

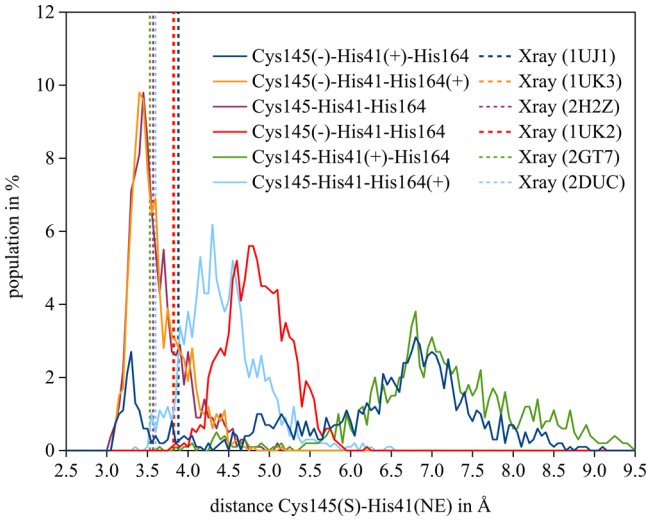

Figure 1. Histogram analysis of the Cys145−His41 distances as obtained from the six MD simulations (solid lines). Histogram profiles refer to the protonation states defined in Scheme 1. Populations of observed distance values were obtained through statistical binning with a resolution of 0.05 Å and are given in relation to the overall number of 1000 measured points (in percent). Experimentally determined values from the six X-ray structures 1UJ1,[3] 1UK3,[3] 2H2Z,[96] 1UK2,[3] 2GT7,[95] and 2DUC[33] are indicated by vertical dashed lines.

between residues His41, His164, and Asp187 (Scheme 1). Averaged values for the four important geometry parameters are summarized in Table 2. To get an estimate of the significance of the structural agreements or disagreements with the experimental values, the average values and standard deviations were calculated for the set of six measurements from the X-ray structures. The averaged distance values from MD simulations were then compared with the experimental standard deviations to decide whether or not they are consistent with the available X-ray structure information. Considering all geometry parameters, we found that only the **Cys145-His41-His164** state is in good agreement with each of the four distance values.

We therefore concluded that the catalytic dyad most likely exists in a neutral (uncharged) resting state **Cys145-His41-His164**, which also conforms to experimentally determined pK_a values of 7.7−8.3 for Cys145 and 6.2−6.4 for His41.[15,27] Furthermore, our MD simulations revealed that His164 is uncharged as well, since protonation of this residue would strongly interfere with the rigid hydrogen network accommodating the buried water molecule H_2O@His41. A further interesting observation relates to the Cys145−His41 distance, which was determined to be in the range of 3.6−3.7 Å. Obviously, this distance is too large to allow direct hydrogen bond interactions between the donating cysteine thiol group and the accepting histidine nitrogen atom, suggesting that the catalytic dyad possesses a bridging water molecule between the two residues, which is in perfect agreement with our simulation trajectory.

Proton-Transfer Potentials. The presence of an uncharged thiol/imidazole state of the SARS-CoV M^{pro} catalytic dyad implies that the enzyme employs a general base-catalyzed mechanism.[27] This usually includes deprotonation of the thiol group, assisted by the neighboring histidine residue, and subsequent attack of the formed thiolate at the electrophilic substrate's amide moiety or, alternatively, at an inhibitor warhead. Theoretical studies have shown that this most likely involves a two-step mechanism of deprotonation and subsequent nucleophilic attack, rather than a (single) concerted reaction.[28] Therefore, the kinetic and thermodynamic characteristics of the initial deprotonation step are of particular interest to understand the mechanisms involved in both enzyme inhibition and substrate cleavage.

For the given case, a QM/MM model system was set up to calculate minimum energy paths of possible proton-transfer reactions within the active site of the SARS-CoV M^{pro}. The topology of the active site (Scheme 1) shows that, beside the proton transfer between Cys145 and His41, a second proton transfer between His41 and His164 could occur which, if confirmed, would be mediated by the buried water molecule H_2O@His41. To evaluate this possible proton relay mechanism, the QM part of the system was set up to include the side chains of Cys145, His41, His164, and the two bridging water molecules, as shown in Figure 2 (right-hand side, top). Parameters for the stationary states I−IV are provided in Table 3 and Scheme 3. The MM part includes an aqueous solvation sphere and both protomers of the dimeric SARS-CoV M^{pro} structure, the latter being of special importance since only the dimeric structure has a catalytically competent conformation.[84,86−88] The QM/MM setup is illustrated below in Figure 3a. In order to "drive" the desired proton-transfer reaction and calculate the respective PES, suitable reaction coordinates had to be determined. The chain of directly involved bond length changes involves as many as eight bonds (four chemical bonds, and four hydrogen bonds) for the given case, as depicted in Figure 2 (right-hand side, top). Nevertheless, most of the bond length changes can be expected

Table 2. Comparison of MD Simulation Results with Available X-ray Structures[a]

	Cys145(S)−His41(NE)			His41(ND)−H_2O(O)			His164(NE)−H_2O(O)			Asp187(OA)−H_2O(O)		
	d	Δ*d*		*d*	Δ*d*		*d*	Δ*d*		*d*	Δ*d*	
X-ray data[b]	3.71	±0.15		2.83	±0.24		3.06	±0.10		2.88	±0.16	
Cys145-His41-His164	3.59	−0.12	(+)	2.90	0.07	(+)	2.96	−0.10	(+)	2.75	−0.13	(+)
Cys145(−)-His41(+)-His164	6.11	2.40	(−)	5.09	2.26	(−)	3.02	−0.04	(+)	2.80	−0.08	(+)
Cys145(−)-His41-His164(+)	3.59	−0.12	(+)	4.84	2.00	(−)	3.77	0.71	(−)	5.57	2.69	(−)
Cys145(−)-His41-His164	4.83	1.13	(−)	2.93	0.10	(+)	2.94	−0.12	(−)	2.79	−0.09	(+)
Cys145-His41(+)-His164	7.10	3.39	(−)	5.07	2.23	(−)	3.05	−0.01	(+)	3.77	0.89	(−)
Cys145-His41-His164(+)	4.41	0.71	(−)	6.57	3.73	(−)	3.21	0.15	(−)	2.91	0.03	(+)

[a]Compared were the mean values of selected geometry parameters of the active site, in Å. Distance values *d* were obtained from MD simulations and calculated as mean values over the whole simulation trajectory of 10 ns. The deviation Δ*d* indicates how this value deviates from the experimental value (mean of six X-ray measurements) that is given in the first row. Positive and negative signs indicate whether the deviation of the simulated mean value Δ*d* ranges within (+) or outside (−) the standard deviation (±) of the X-ray reference value. [b]Mean values and standard deviations (±) from the set of six X-ray structures 1UJ1,[3] 1UK3,[3] 2H2Z,[96] 1UK2,[3] 2GT7,[95] and 2DUC.[33]

dx.doi.org/10.1021/bi400604t | *Biochemistry* 2014, 53, 5930−5946

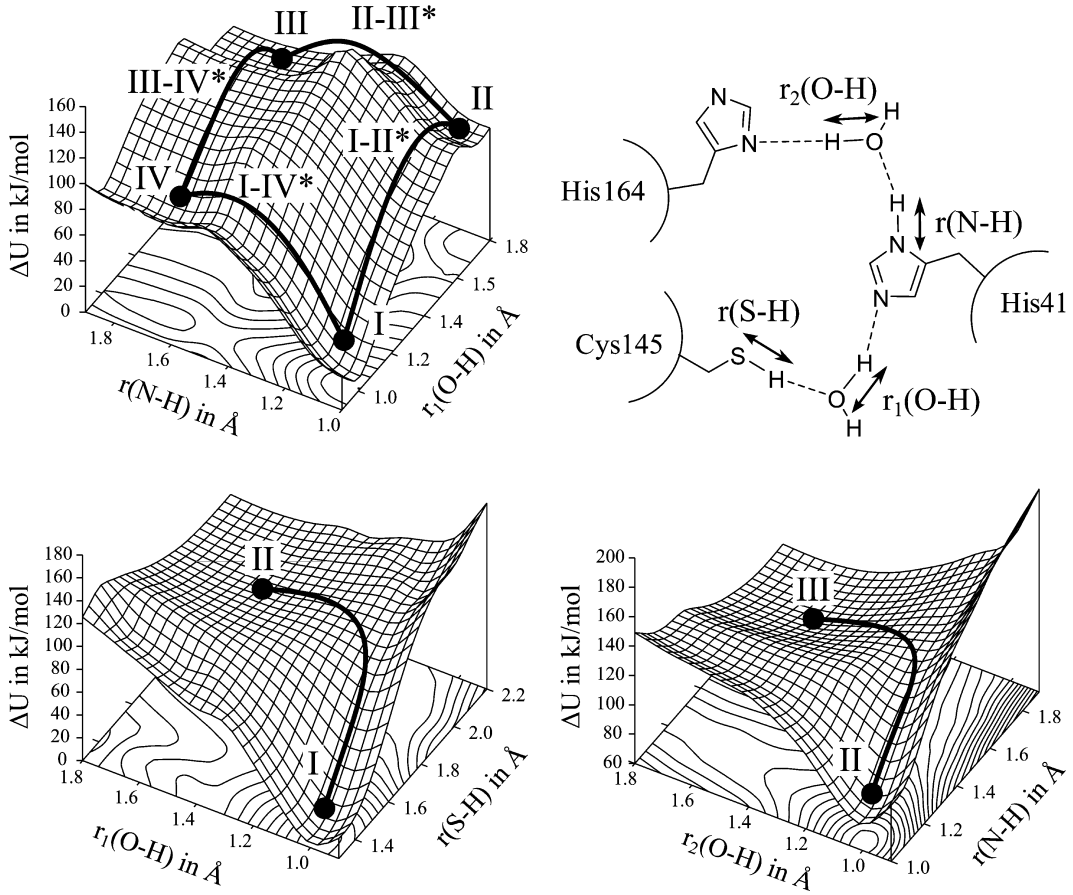

Figure 2. Calculated QM/MM potential energy surfaces (PESs) of the different protonation states of SARS-CoV M^{pro} active-site residues Cys145, His41, and His164. Proton transfers are mediated by two bridging water molecules. All energies are given in kJ/mol. I–IV as defined in Table 3. PESs refer to the free enzyme QM/MM system (a) (see Figure 3) in the absence of inhibitor or substrate bound to the active site. The employed QM subsystem and reaction coordinates that were used for "driving" the proton-transfer reactions are given at the top on the right-hand side. The reaction coordinates r_1(O–H) and r(S–H) (left-hand side, bottom) and further r_2(O–H) and r(N–H) (right-hand side, bottom) were smoothly coupled to each other and, therefore, it was considered sufficient to use only one of these coordinates for the proton transfers between Cys145/His41 and His41/His164. The PES on the left-hand top side combines the Cys145/His41 proton transfer by using ther_1(O–H) coordinate on the first axis and the His41/His164 proton transfer by using the r(N–H) coordinate on the second axis, providing relative energies for the four different protonation states I–IV and their respective transition states.

Table 3. Located Minima and Maxima on the Potential Energy Surface (Figure 2, left-hand side, top) and Their Relative Energies Δ*U* with Respect to the Neutral State Cys145-His41-His164 (I) in kJ/mol

minima			transition states		
point	refers to state	Δ*U*	point	refers to transition	Δ*U*
I	**Cys145-His41-His164**	0	I–II*	**Cys145-His41-His164** to **Cys145(−)-His41(+)-His164**	101
II	**Cys145(−)-His41(+)-His164**	87	II–III*	**Cys145(−)-His41(+)-His164** to **Cys145(−)-His41-His164(+)**	117
III	**Cys145(−)-His41-His164(+)**	90	III–IV*	**Cys145(−)-His41-His164(+)** to **Cys145-His41(−)-His164(+)**	123
IV	**Cys145-His41(−)-His164(+)**	75	I–IV*	**Cys145-His41-His164** to **Cys145-His41(−)-His164(+)**	84

to be correlated with each other. To evaluate this, the two transitions between the **Cys145-His41-His164** to **Cys145(−)-His41(+)-His164** states (Figure 2, left-hand side, bottom) and the **Cys145(−)-His41(+)-His164** to **Cys145(−)-His41-His164(+)** state (Figure 2, right-hand side, bottom) have been calculated separately in individual PES calculations. They comprise two reaction coordinates, respectively, one for the deprotonation of the amino acid moiety, and one for the deprotonation of the bridging water molecule. The shape of the two PESs (Figure 2, bottom) shows that both minimum energy paths proceed in a concerted way, without the occurrence of (meta)stable H_3O^+ intermediates. Therefore, the proton-transfer reactions for the **Cys145-His41-His164** to **Cys145(−)-His41(+)-His164** transition and the **Cys145(−)-His41(+)-His164** to **Cys145(−)-His41-His164(+)** state can be described by using only one coordinate for each transition, since all other bond lengths follow smoothly according to this coordinate and are therefore directly correlated to each other.

For the description of the whole charge-relay mechanism (Figure 2, left-hand side, top) the r_1(O–H) and the r(N–H) coordinates were selected. From the PES, four local minimum states I–IV could be found, which are connected to each other by definite transition state passes. The relative energies Δ*U* of the located minima and maxima with respect to the state of lowest energy **Cys145-His41-His164** (I) are summarized in Table 3. The thermodynamic equilibrium between the **Cys145(−)-**

dx.doi.org/10.1021/bi400604t | *Biochemistry* 2014, 53, 5930–5946

Scheme 3. Charge Deletion Analysis and Topology of the SARS-CoV M^{pro} Active Site with the Catalytic Dyad in the Zwitterionic State Cys145(−)-His41(+)-His164[a]

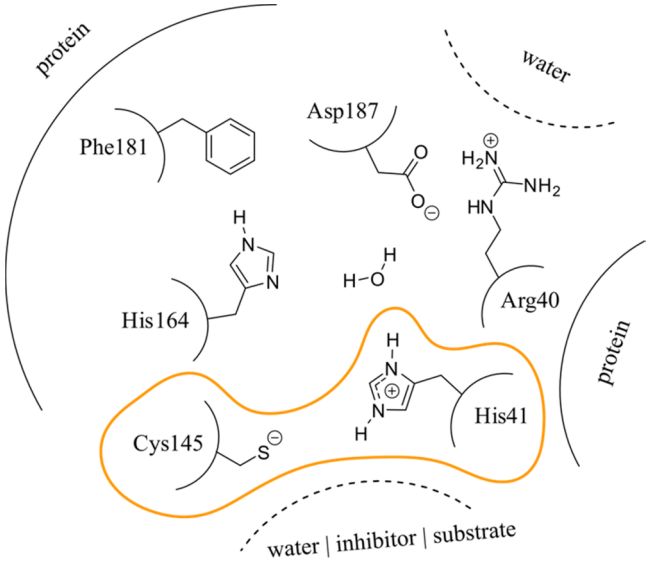

[a]The charges of different neighboring structure elements in the MM subsystem were switched off individually, and their energetic impact on the QM subsystem was estimated as given in Table 4.

His41(+)-His164 zwitterion II and the relayed **Cys145(−)-His41-His164(+)** zwitterion III is nearly balanced with relative energies ΔU = 87 and 90 kJ/mol. However, the kinetic parameters for the transition between the two zwitterionic states differ, since the minimum energy pass I−II* is located at 101 kJ/mol and II−III* at 117 kJ/mol, suggesting that the formation of the unrelayed zwitterion **Cys145(−)-His41(+)-His164** is kinetically preferred.

Interestingly, the possibility of a further, and rather unexpected, zwitterionic state comprising the formation of a histidine anion and histidine cation could be observed. Although the **Cys145-His41(−)-His164(+)** state IV seems to be an appealing route with quite preferable kinetic (ΔU = 84 kJ/mol) and thermodynamic (ΔU = 75 kJ/mol) parameters, it represents a dead-end process, since the formation of the Cys145 thiolate would have to overcome a barrier of 123 kJ/mol (III−IV*) to become anionic. Taking these things together, the formation of the nonrelayed zwitterion **Cys145(−)-His41(+)-His164** appears to be the most likely situation, although the transition state of 101 kJ/mol (I−II*) for the minimum energy path to state I appears quite high compared to related enzymatic proton-transfer reactions.[89−93] The route to the charge-relayed zwitterion **Cys145(−)-His41-His164(+)** is therefore even more unlikely. Furthermore, a CoV-wide comparative sequence analysis of main proteases (data not shown) revealed that, in about two-thirds of coronavirus main proteases, the SARS-CoV M^{pro} His164 residue is substituted with Gln, arguing against a key role of a protonated His164 residue in catalyzis.

Our investigations outlined above predict a prohibitively high barrier for the formation of the zwitterion state **Cys145(−)-His41(+)-His164** whose formation, however, is a prerequisite for proteolysis.[44] It was therefore necessary to investigate if the proton transfer becomes more favorable through substrate or inhibitor binding. Fortunately, extensive structural data of SARS-CoV M^{pro} are available from X-ray crystallography studies, which also include complexes with inhibitors[3,5,94−105] and a substrate.[6] Based on these data, the proton-transfer potentials for the free enzyme, the inhibitor-bound enzyme, and the substrate-bound enzyme were compared using identical computational QM/MM workflows. For the complexed inhibitor, a high-resolution structure with an α,β-unsaturated ester compound was selected (PDB code 2DUC[33]) because this warhead type has been extensively characterized by many studies over the past years. The substrate complex (PDB code 2Q6G[6]) included the amino acid sequence Ser-Ala-Val-Leu-Gln-l-Ser-Gly-Phe, which represents a natural substrate sequence of the SARS-CoV M^{pro}.[106] For the free SARS-CoV M^{pro} (no substrate or inhibitor), the same structure as described above for the PES calculations was used. Prior to the QM/MM computations, 10 ns MD simulations were conducted for each of the three systems to generate an extensive set of starting structures for the QM/MM minimum path calculations.

To take structural fluctuations during an MD run into account, the proton-transfer potentials were averaged starting from 11 snapshots for each of the three model systems. To help identify meaningful connections between the two minima, proton-transfer potentials were furthermore assessed by calculations in forward and backward directions. The SARS-CoV M^{pro} X-ray structures of the inhibitor complex and the substrate complex revealed that the Cys145/His41 distance is slightly closer than in the free enzyme, indicating that, in these cases, the catalytic dyad is unlikely to be bridged by a water molecule. This could also be confirmed by visual inspection of the MD simulation trajectories, which consistently and exclusively suggested a direct hydrogen bond between the thiol group and the accepting nitrogen atom. Figure 3 gives an overview of the three QM/MM model systems. The QM parts include the water-bridged catalytic residues Cys145/His41 for the free enzyme (Figure 3a) and the directly hydrogen-bonded counterparts for the respective complexes (Figure 3b,c).

By comparing the averaged QM/MM potential energy curves of the proton transfer, as given in Figure 4, an interesting effect was observed. For the free enzyme, the averaged proton-transfer potential resulted in a barrier of 70 kJ/mol and a relative energy of 67 kJ/mol for the transition from **Cys145-His41** to **Cys145(−)-His41(+)** which is 20−31 kJ/mol lower than the values obtained for the single PES in Figure 2. This result again illustrates the benefit of averaging minimum energy paths, which provide a better estimate compared to that obtained from single paths.

The proton-transfer potential calculated for the inhibitor-bound structure was found to be in a similar range with a barrier of 63 kJ/mol and a relative energy of 69 kJ/mol for **Cys145(−)-His41(+)**. Interestingly, however, for the substrate-bound model system, significantly lower relative energies were determined, with $\Delta U \approx$ 38 kJ/mol in the zwitterionic region. Furthermore, there was no separating barrier between **Cys145-His41** and **Cys145(−)-His41(+)** in the substrate-bound state of the SARS-CoV M^{pro}.

These data lead us to suggest that substrate binding may have a modulating effect on the proton-transfer potential. This effect was not observed in the inhibitor-bound complex. The hypothesis of a modulating effect is also supported by the standard deviations shown in Figure 4, which provide a good estimate of the fluctuations of potentials determined for a specific set of calculated proton-transfer paths (Figure 4). While the substrate-bound model system revealed a clearly defined average path, indicating little fluctuation, the free and inhibitor-bound enzymes exhibited large standard deviations, indicating quite

dx.doi.org/10.1021/bi400604t | Biochemistry 2014, 53, 5930−5946

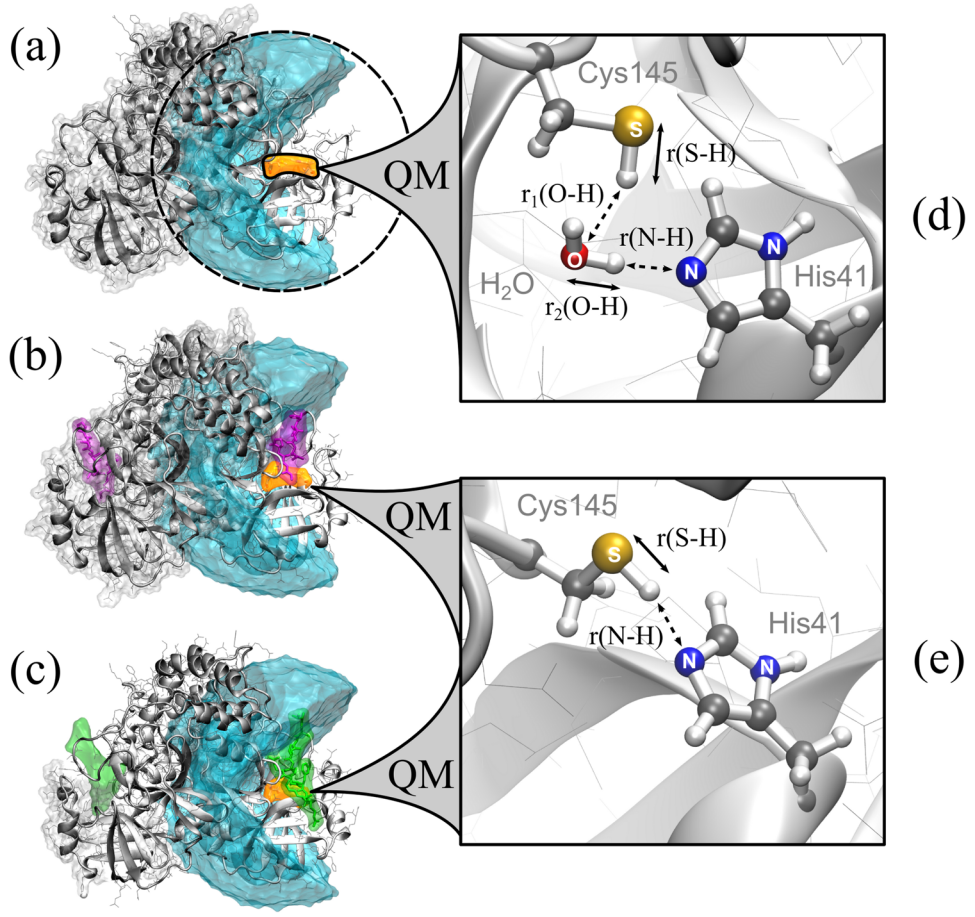

Figure 3. QM/MM model systems employed in this study. The MM subsystems (left)) include the dimeric protein structure of SARS-CoV M^{pro} (gray) and the solvation spheres around the active site (cyan). Three different models were employed. They describe the free enzyme (a) based on X-ray structure 2DUC,[33] the enzyme with a Michael acceptor inhibitor (magenta) bound to the active site (b) based on X-ray 2AMD,[5] and the enzyme with a natural substrate peptide (green) bound to the active site (c) based on X-ray 2Q6G.[6] QM subsystems (orange) include the active-site residues Cys145 and His41 without backbone atoms and are either bridged with a water molecule (d) or directly hydrogen-bonded to each other (e). Reaction coordinates are indicated with arrows and show the coordinates that are used to drive the proton transfer (solid lines). Also shown are the coordinates that smoothly follow the driving reaction coordinates (dashed lines) on the potential energy surface.

significant fluctuation. These data are consistent with our hypothesis that substrate binding by the M^{pro} facilitates formation of the **Cys145(−)-His41(+)** zwitterion in the active site.

Charge Deletion Analysis. The results obtained by the QM/MM potentials provided an estimate of 25−30 kJ/mol for the stabilization of the zwitterion due to substrate binding in the active site of the SARS-CoV M^{pro}. In order to further dissect these stabilizing contributions, a CDA was performed for the three QM/MM model systems. It should be noted that the CDA only accounts for the electrostatic interactions and not for other intermolecular interactions, such as exchange or dispersion interactions which, for example, might play a role for phenyl rings. Nevertheless, electrostatic contributions typically possess the greatest impact among the intermolecular interactions due to their $1/r^2$ distance-dependent behavior. Since possible pitfalls from single minimum energy path calculations,[70−73] as described above, equally apply to CDA, an analogue averaging was performed over 11 snapshots for each case. CDA was performed for the local minimum states **Cys145-His41** and **Cys145(−)-His41(+)**. $\Delta\Delta U$ values were calculated by subtraction, yielding the respective energetic impact on the zwitterionic state (Scheme 3). A more detailed description of the procedure is given in the computational details section. Table 4 summarizes the results obtained from the CDA including the electrostatic contribution of various parts of the environment with standard deviations obtained from data sets of 11 averaged snapshots.

The protein environment was found to be the major contributing factor in stabilizing the **Cys145(−)-His41(+)** state by 18−31 kJ/mol, depending on the model system. The other protomer in the dimer was found to have practically no impact on the proton-transfer reaction. A detailed examination of single active-site residues was then performed to gain more insight into their individual roles in the first step in catalyzis.

The calculated impact of just 1−7 kJ/mol for His164 shows that this histidine residue plays no important role in the formation of **Cys145(−)-His41(+)**. Switching off Arg40 revealed that this residue could significantly contribute to the zwitterionic state, with a stabilizing effect of 17−19 kJ/mol observed in the absence of this residue. Scheme 3 shows the relative orientation of Arg40 with respect to the dipole formed by the zwitterionic catalytic dyad. The positive charge of the arginine residue is located in close proximity to the positively charged His41 residue. Withdrawal of one of the positive charges is expected to decrease the electrostatic repulsion, thus stabilizing the **Cys145(−)-His41(+)** state. Removal of Asp187 has an opposite effect because the negative charge of the carboxylate group has an important stabilizing effect on zwitterion formation.

dx.doi.org/10.1021/bi400604t | *Biochemistry* 2014, 53, 5930−5946

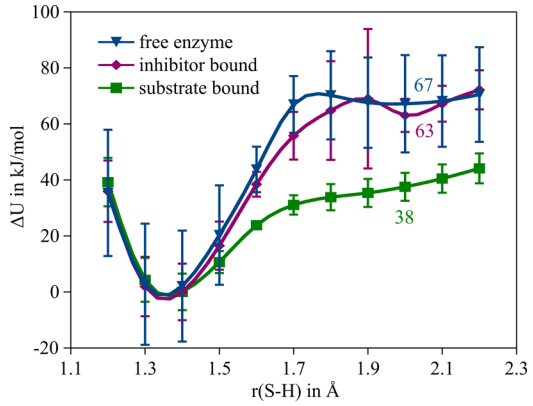

Figure 4. Averaged QM/MM potential energy curves of the proton transfer between Cys145 and His41 for the three model systems (a–c in Figure 3), comparing the free enzyme (blue line), inhibitor-bound enzyme (magenta line) and substrate-bound enzyme (green line), as shown in Figure 3. Energy values (in kJ/mol) are given relative to the neutral state **Cys145-His41-His164**. The averaging was done for 20 potentials aligned by least-squares fitting and based on minimized snapshots of 10 ns MD simulations for each model system. Standard deviations for each point are indicated by vertical bars. The reaction coordinate r(S–H), as shown in Figure 3d,e, was used to attain the proton transfer between the **Cys145-His41-His164** and **Cys145(−)-His41(+)-His164** states.

Table 4. Charge Deletion Analysis[a]

	ΔΔU(ZW)		
residue switched off	free enzyme[b]	inhibitor-bound[c]	substrate-bound[d]
protein	31 ± 16.5	22 ± 10.6	18 ± 7.0
protomer A	27 ± 16.0	18 ± 11.6	20 ± 6.2
protomer B	4 ± 1.5	1 ± 0.8	−4 ± 3.6
His164	1 ± 3.8	7 ± 2.3	5 ± 3.6
Arg40	−17 ± 2.7	−19 ± 1.2	−18 ± 2.2
Arg40-Asp187	8 ± 5.0	9 ± 1.5	3 ± 2.0
Asp187	23 ± 5.7	26 ± 0.9	19 ± 1.4
Phe181	0 ± 0.1	0 ± 0.2	0 ± 0.2
H_2O@His41	18 ± 4.4	14 ± 1.4	0 ± 0.1
water	−5 ± 63.4	18 ± 5.3	25 ± 11.0
substrate			8 ± 3.1
inhibitor		−1 ± 3.9	

[a]Energy values ΔΔU, in kJ/mol, refer to the change in energy that occurs due to switching off certain parts of the QM/MM system with respect to the unaffected QM/MM system, as shown in Scheme 3. Values ΔU(ZW) refer to the relative energy of the zwitterionic state **Cys145(−)-His41(+)-His164** compared to the neutral state **Cys145-His41-His164** of the catalytic dyad. [b]Data set consists of 11 minimized snapshots taken from MD simulation based on 2DUC.[33] [c]Data set consists of 11 minimized snapshots taken from MD simulation based on 2AMD.[5] [d]Data set consists of 11 minimized snapshots taken from MD simulation based on 2Q6G.[6]

By removing this moiety, the favorable interaction between the negative charge of Asp187 and the positive charge of His41 is disturbed, increasing the relative energy by 19–26 kJ/mol for **Cys145(−)-His41(+)** compared to **Cys145-His41**. If Arg40 and Asp187 residues are considered together as a salt bridge, the two residues only have a marginally stabilizing effect of 3–9 kJ/mol on zwitterion formation. The idea that the salt bridge and the zwitterion act as single dipoles is also consistent with the three-dimensional structure of the active site. Here, the two dipoles are oriented nearly perpendicular to each other, with Asp187 being slightly closer to the catalytic dyad. The Asp187–Arg40 salt bridge essentially abolishes the individual stabilizing and destabilizing effects of Asp187 and Arg40, respectively. Nevertheless, Asp187 appears to play the most important role in the closer neighborhood of the active site and likely has a role in the first step of the general base catalyzis of SARS-CoV M^{pro}.

The Phe181 has no impact in the CDA, since its phenyl ring side chain has no significant electrostatic influence. However, a contribution of this residue cannot be completely excluded because interactions between aromatic systems and cationic histidines are well documented[107] and may have stabilizing effects of ∼4 kJ/mol,[108] depending on the spatial orientation of the residues involved.[109]

Taken together, all these protein-related contributions were consistently found for the three model systems, but most of these changes were not statistically significant.

However, regarding the influence of water, a different trend is observed. Water has a two-fold role in SARS-CoV M^{pro} catalyzis. It acts both as a part of the solvent shell and an inherent and conserved part of the active site as revealed by all X-ray structures available to date. With respect to the buried water molecule sitting between His41, His164, and Asp187 (H_2O@His41), a decreasing importance for the stabilization of the zwitterion was observed, with contributions of 18, 14, and 0 kJ/mol, when calculations were performed for the free enzyme, inhibitor-bound enzyme and substrate-bound enzyme, respectively. Since it was present in all MDs of the three model systems and did not drift out of the rigid hydrogen bond network, as occasionally hypothesized in the literature,[84,110] the cause of this effect may be attributed to substrate-induced changes of the active site conformation and, more specifically, local adjustments of the various stabilizing effects that contribute to zwitterion formation.

Even more interesting is the role of the water shell. Comparison of the three model systems revealed that the contribution of the solvation sphere to the formation of the zwitterion differs quite significantly between the free enzyme and the two complexes. In the first case, the averaged view reveals a marginally destabilizing effect on the formation of **Cys145(−)-His41(+)-His164**, reflecting that the proton-transfer path has to proceed through a rigid hydrogen bond network formed by the first solvation shell. This first solvation shell, which may also be called biological water,[111−113] has a constitution that corresponds to the **Cys145-His41** state and can hardly adopt the **Cys145(−)-His41(+)** state that is instantaneously formed by following the minimum energy path. The extremely high standard deviation of 63 kJ/mol shows that already small changes in the first solvation sphere have a strong impact on the proton-transfer potential. The situation is quite different for the enzyme–substrate complex. In this case, the first solvation sphere seems to be well shielded through the substrate so that only the stabilizing effect of the water bulk remains. It fosters the formation of **Cys145(−)-His41(+)** by 25 kJ/mol. Furthermore, significantly less fluctuation from this contribution (standard deviation ≈ 11 kJ/mol) was observed when compared to the free enzyme. For the inhibitor-enzyme complex a similar situation is predicted; however, the shielding through the inhibitor seems to be less effective.

This interpretation of the CDA data is supported by Figure 5, which shows the coverage of the active site by inhibitor and substrate (upper part) and the radial pair distribution functions RDF of solvent water around the active-site residues His41 (left-hand side) and Cys145 (right-hand side). Distances were calculated for 1000 frames with the respective analysis tool in

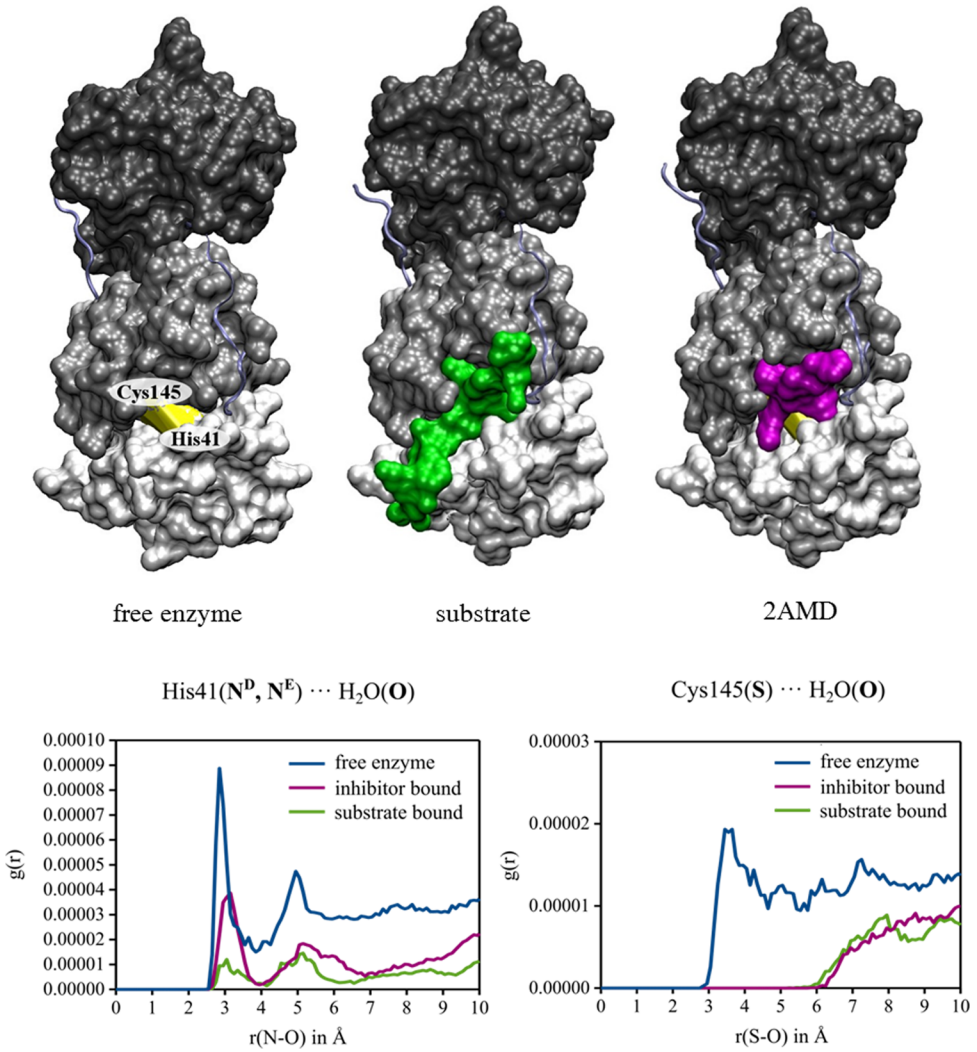

Figure 5. Upper part: Coverage of the active site (yellow) by the substrate (green) and the inhibitor (magenta). For the free enzyme the positions of the Cys145 and the His41 moiety are indicated. Lower part: Radial pair distribution functions of solvent water around the active site residues His41 (left-hand side) and Cys145 (right-hand side).

VMD.[39] Distributions for His41 include pair distances between nitrogen atoms (ND and NE) and all solvent water oxygen atoms. Distributions for Cys145 include pair distances between the sulfur atom and all solvent water oxygen atoms. For the free enzyme, both moieties are surrounded by water molecules. Both the coverage picture and RDF show consistently that substrate and inhibitor shield the Cys145 residue very efficiently from the water shell. For the His41 residue, however, the differences are obvious. The incomplete coverage of the His41 residue through the inhibitor seems to be responsible for the differences discussed above.

Finally, Table 4 shows that the inhibitor does practically not influence the **Cys145-His41/Cys145(−)-His41(+)** equilibrium, whereas the substrate contributes 8 kJ/mol to support zwitterion formation. Although this difference is rather small, it may be an inherent property of the substrate that is not featured by the inhibitor. If confirmed, this observation may have interesting implications for inhibitor design.

Free Energy Calculations. Although the conducted QM/MM minimum path calculations allow deep insights into the proton-transfer reaction, they provide a static picture of the model systems and do not account for dynamics or entropic effects. PMF-based free energy calculations are a commonly used approach to overcome this deficiency.[114−116] They have also become popular in combination with the QM/MM methodology.[63,117−119] Furthermore, from a theoretical perspective, the calculation of free energies is very well suitable to complement minimum energy path calculations.

To get access to the free energy profiles of the proton transfer, the model systems of the free enzyme and the substrate-bound complex were set up for QM/MM MD simulations, in an identical manner to the previous QM/MM calculations, as shown in Figure 3a,c. Since extensive sampling is necessary to obtain a PMF, a semiempirical method (PM3/PDDG) instead of density functional theory had to be employed to keep the computational efforts feasible. Please note that PM3/PDDG overestimates the difference between the neutral and the zwitterionic state by 38 kJ/mol in comparison to B3LYP/TZVP, which was employed for the QM/MM minimum path calculations.[44]

Figure 6 shows the free energy potentials for the free enzyme model (blue) and the substrate-bound model (green), as obtained by the PMF. The relative free energies ΔG of **Cys145(−)-His41(+)-His164** with respect to the neutral state **Cys145-His41-His164** are quite similar for both cases, with free energy values of 73 kJ/mol for the free enzyme and 67 kJ/mol for

dx.doi.org/10.1021/bi400604t | *Biochemistry* 2014, 53, 5930−5946

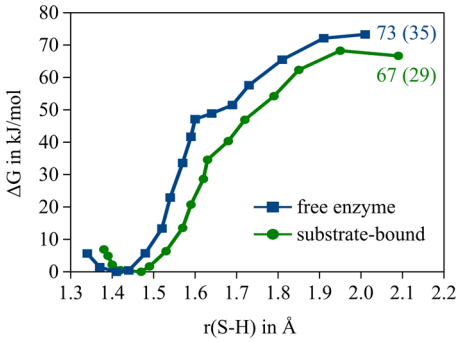

Figure 6. Free energy potentials of the proton transfer between the **Cys145-His41-His164** and the **Cys145(+)-His41(+)-His164** state, in kJ/mol. The free enzyme (blue line), as shown in the QM/MM model in Figure 3a, and the substrate-bound (green line) QM/MM model, as shown in Figure 3c, were compared. The r(S−H) distance given in Figure 3d,e served as reaction coordinate. Values ΔG were obtained by the potential of mean force method, employing PM3-PDDG, by using samplings of 50 ps for each point with a subsequent weighted histogram analysis. The values shown in parentheses represent corrected values. For more information see text.

the substrate-bound case, respectively. Taking into account the error made by PM3/PDDG, the corrected free energy PM3/PDDG results for the substrate-bound PMF (ΔG = 29 kJ/mol) agree quite well with the B3LYP/TZVP minimum path calculations (ΔU = 38 kJ/mol). The remaining difference of 9 kJ/mol can be considered as insignificant due to the inaccuracy of the methods.

The situation changes for the free enzyme model. Whereas the B3LYP/TZVP QM/MM minimum path calculations predict ΔU = 67 kJ/mol between neutral and zwitterionic state, the PM3/PDDG free energy, corrected to the B3LYP/TZVP level ΔG, is only about 35 kJ/mol, i.e., $\Delta G < \Delta U$. Several reasons can be responsible for this stabilization of the zwitterionic state by 32 kJ/mol. The error bars of both methods may contribute to the difference. However, in our opinion, the difference is too large to solely represent an artifact. The next reason refers to entropic effects that are only accounted for in the free energy calculations. Since the entropic effects found for the protein−substrate complex are rather small,[72,120] the change would have to result from the inner water-shell which reorients due to the emerging zwitterionic state. Since the interaction between solvent water molecules and the zwitterionic centers should be stronger than the corresponding interactions with the neutral centers, the solvent shell of the zwitterionic state should have a higher order than the solvent shell of the neutral state. Since the order increases, ΔG should be more positive than ΔU; however, the opposite is found here. Hence, even though entropic effects may contribute, they do not seem to be the main reason for the stabilization of the zwitterionic state.

The second reason for the additional stabilization of the zwitterionic state is the possibility of a relaxation of the inner solvation sphere as a function of the emerging zwitterionic state. Clearly, QM/MM MD sampling allows a much better relaxation of the first solvation sphere, since it provides 50 ps of MD simulation in which barriers to lower minima can be surmounted. In the QM/MM minimum path calculations, the relaxation is considerably restricted since the water molecules can only relax to the next local energy minimum but not surmount any barriers to reach deeper ones. Since the computations start from the neutral state, better relaxation possibilities clearly favor the zwitterionic state compared to the neutral one. Hence, this second reason seems to be more important, since QM/MM MD indeed predict a more stabilized zwitterionic state than QM/MM minimum path computations. This is supported by QM/MM MD calculations with simulation times of 25, 50, and 100 ps which predicted energy differences of 23, 20, and 17 kJ/mol, respectively. A plot of the results can be found in the Supporting Information. QM/MM minimum path calculations only take into account solvent relaxations that happen on a very fast time scale, e.g. the polarization of the electron clouds of the water molecules and some small fast motions while QM/MM MD simulations can also be used to assess relaxation processes that take place on considerably longer time scale.

These considerations indicate that the zwitterionic state is considerably stabilized if the inner water shell has the possibility to relax. This however implies that the zwitterionic state would only be stabilized if this relaxation proceeded on a shorter time scale than the proton transfer itself. Proton-transfer reactions are assumed to take place on sub-picosecond time scales.[121,122] The relaxation of bulk water has relaxation times of <10 ps;[123] that is, it proceeds with similar speed or even slightly more slowly than the proton-transfer process. Under the heading "biological water",[111−113] it has been proposed that water molecules at the surface of proteins even need times in the range of 8−80 ps to reorient.[111] Therefore, they definitely would be to slow to contribute to the stabilization of the zwitterionic state.

To summarize these points together with the remaining errors of the B3LYP/TZVP approach (−17 kJ/mol with respect to a LCCSD(T)/QZVP computation), our computations indicate that for the free enzyme the energy difference between the neutral and zwitterionic states is between 84 kJ/mol (corrected QM/MM minimum energy path computation) and 59 kJ/mol (corrected QM/MM MD simulations). Since the water relaxation seems to proceed on a similar or even longer time scale than the proton-transfer reaction, the energy difference should be closer to the higher value.

The situation differs for the enzyme−substrate complex. Taking into account the remaining errors of the B3LYP/TZVP approach, both the QM/MM MD and QM/MM minimum energy path computations predict an energy difference of only about 46 kJ/mol. Due to this reduction, the substrate strongly promotes the proton transfer and, as a consequence, its own proteolysis since the proton transfer is a prerequisite of the overall reaction.

Free energy calculations of the corresponding inhibitor reaction are impossible due hardware and software limitations. However, since the static calculations predict an energy difference between the neutral and zwitterionic states that resembles that computed for the free enzyme, we expect similar behaviors for both systems. Also in the free energy calculation of the inhibitor-enzyme complex, the environment will adapt to the changing electronic structure of the active site so that the free energy difference is lower than the static energy difference. However, as discussed for the free enzyme, it can be assumed that the proton transfer will again be faster than the adaptation. If no adaption of the environment can take place, the energy difference obtained from the free energy calculation will resemble the value obtained from the static calculation, which is too large for an efficient proton transfer. This indicates that, in contrast to the substrate, the inhibitor is not able to catalyze the proton transfer. In other words, the inhibitors block the active site but their covalent reactions with the enzyme are not so fast, and thus very moderate overall inhibition potencies result.

dx.doi.org/10.1021/bi400604t | *Biochemistry* 2014, 53, 5930−5946

The difference between the substrate and the inhibitor reaction becomes clear if we compare k_{cat} data with the k_i values given in Table 1. Okomoto et al.[16] measured 3.3 ± 0.14 s^{-1} for k_{cat}, while Solowiej et al.[15] report values of around 0.6−0.9 s^{-1}. Both values are 2−3 orders of magnitude larger than the k_i value of 0.0022 s^{-1} which was measured for the inhibitor under consideration (2AMD). This inhibitor contains an α,β-unsaturated ester as warhead (see Table S1 in the Supporting Information for the Lewis structures of the inhibitors).

Our findings are in line with the assumption of an "electrostatic trigger" that initiates the catalytic reaction, as reported in the work of Solowiej et al.[15] Moreover, our simulations provide an atomistic picture of the underlying interactions. They furthermore support the conclusion of Okamoto et al.,[16] who noted that their investigations indicate "a further fine-tuning mechanism for biological control, particularly in the micro-environment".

A comparison of different inhibitors indicates that our findings about the interplay between coverage and reactivity of the active site may be applicable more widely than initially thought. The chemical structures and with this the reactivities of the 2A5I and 2OP9 inhibitors, which both possess an epoxide as warhead, are very similar. The corresponding k_i values (0.035 vs 0.004 s^{-1}) differ, however, by about one order magnitude. The higher value for 2A5I may result from a more complete coverage of the active site compared to the area covered by the 2OP9 inhibitor (Table S3 in the Supporting Information). A similar correlation was found when we compared the 2HOB (Table S3) and the 2AMD inhibitor (Figure 5) which both possess α,β-unsaturated esters as warheads. The inhibitor 2V6N, which shows nearly no coverage of the active site (Table S3) but has a k_i value of 0.013 s^{-1}, is a special case. It possesses a benzotriazole ester as warhead which is known to be an active ester used as activated carboxylic acid component in peptide and ester syntheses and which is considerably more reactive than the other warheads.[124] We would like to point out that our findings essentially depend on visual inspections and remain to be substantiated by further simulations, which will be the subject of future work.

It is important to note that experimentally available pK_a measurements of SARS-CoV M^{pro} estimate the relative free energy between the neutral and the zwitterionic states to be 7−12 kJ/mol, which is considerably lower than our values. The differences may result from deficiencies of the applied QM/MM models. However, we would like to point out that pK_a values represent thermodynamic quantities; i.e., the solvent shell can perfectly adapt to a given situation. However, as discussed above, this seems not to be the case for the proton-transfer reaction. Perfectly adapted solvent shells are better reflected by solvent continuum models. For our system they predict an energy difference of only 34 kJ/mol, i.e., lower than the values discussed above.[44] Further reductions of the difference between our theoretical studies and previously published experimental data may result from directed hydrogen bonds, which should further stabilize the zwitterionic state and are often underestimated in continuum models. Furthermore, the remaining difference may also result from the fact that pK_a measurements reflect proton exchange reactions of single centers with solvent water molecules, while our simulations concentrate on the proton exchange reaction between both centers.

CONCLUSIONS

In summary, the active site of the SARS-CoV M^{pro} was characterized from different theoretical perspectives. The comparative analysis of several MD simulations with available structural data from X-ray crystallography revealed that the catalytic dyad of SARS-CoV M^{pro} has a neutral charge state and also the neighboring His164 residue appears to be uncharged. Although His164 could act as a proton acceptor through a hypothetical charge-relay mechanism, both the results from QM/MM potential energy surface calculations and the replacement of this residue with Gln in other coronavirus main proteases suggest that this is an unlikely scenario.

The comparison of free enzyme, inhibitor-bound enzyme, and substrate-bound enzyme by averaged QM/MM potentials and QM/MM MD simulations has shown that the necessary proton-transfer reaction toward the formation of an ion pair is remarkably facilitated by substrate binding. It reduces the energy difference between neutral and zwitterionic states (which is an important part of the energy barrier to be overcome during proteolysis) to about 46 kJ/mol. This indicates that the catalytic dyad is "switched on" through substrate binding; i.e., the substrate itself contributes to the catalyzis of its proteolysis reaction. This is supported by charge deletion analyses and the computed structures. The former predict a stabilizing effect of the substrate for the zwitterionic state, and the latter show a very efficient coverage of the active site by the natural substrate. Hence, proteins which enter the active site but take different positions than the natural substrates should not be able to lower the energy difference and, consequently, do not react. This indicates an interesting interplay between activation of the catalytic center and substrate selectivity of the SARS-CoV M^{pro}. It remains to be seen if similar mechanisms are operational in other viral and cellular proteases. Our study also adds to the growing list of examples for solvent water playing an active role in enzyme catalyzis rather than being a more or less innocent bystander.[125,126]

The importance of the position of the ligand is supported by computations for the enzyme−inhibitor complex, which did not reveal a similar facilitation of zwitterion formation. The development of inhibitors which mimic the ability of the substrate to shield the active site from the solvent shell may therefore be a possible way to improve inhibitors in future studies.

ASSOCIATED CONTENT

Supporting Information

Individual time-dependent RMSD plots for the six comparative MD simulations; plots of proton-transfer potentials as obtained from PMF test calculations with different sampling length of 25, 50, and 100 ps; full PMF free energy surface of water-mediated proton transfer in the free enzyme model; additional information about the inhibitors, including the chemical structure and kinetic parameters; peptide sequences and kinetic parameters; and coverage of the active site by different inhibitors. This material is available free of charge via the Internet at http://pubs.acs.org.

AUTHOR INFORMATION

Corresponding Author

*Phone: (+49)931 31-85394. Fax: (+49)931-888-5331. E-mail: bernd.engels@mail.uni-wuerzburg.de.

Funding

Financial support by the Deutsche Forschungsgemeinschaft within the framework of the SFB 630 "Recognition, Preparation and Functional Analysis of Agents against Infectious Diseases" and of the Volkswagen Stiftung is gratefully acknowledged.

Notes

The authors declare no competing financial interest.

■ ABBREVIATIONS

CDA charge deletion analysis; CoV coronavirus; MD molecular dynamics; MM molecular mechanics; M^{pro} main protease; PES potential energy surface; PMF potential of mean force; QM quantum mechanics; RMSD root-mean-square deviation; SARS severe acute respiratory syndrome

■ REFERENCES

(1) Thiel, V., Ivanov, K. A., Putics, Á., Hertzig, T., Schelle, B., Bayer, S., Weißbrich, B., Snijder, E. J., Rabenau, H., Doerr, H. W., Gorbalenya, A. E., and Ziebuhr, J. (2003) Mechanisms and enzymes involved in SARS coronavirus genome expression. *J. Gen. Virol. 84*, 2305−2315.

(2) Anand, K., Ziebuhr, J., Wadhwani, P., Mesters, J. R., and Hilgenfeld, R. (2003) Coronavirus Main Proteinase (3CLpro) Structure: Basis for Design of Anti-SARS Drugs. *Science 300*, 1763−1767.

(3) Yang, H., Yang, M., Ding, Y., Liu, Y., Lou, Z., Zhou, Z., Sun, L., Mo, L., Ye, S., Pang, H., Gao, G. F., Anand, K., Bartlam, M., Hilgenfeld, R., and Rao, Z. (2003) The crystal structures of severe acute respiratory syndrome virus main protease and its complex with an inhibitor. *Proc. Natl. Acad. Sci. U.S.A. 100*, 13190−13195.

(4) Bartlam, M., Yang, H., and Rao, Z. (2005) Structural insights into SARS coronavirus proteins. *Curr. Opin. Struct. Biol. 15*, 664−672.

(5) Yang, H., Xie, W., Xue, X., Yang, K., Ma, J., Liang, W., Zhao, Q., Zhou, Z., Pei, D., Ziebuhr, J., Hilgenfeld, R., Yuen, K. Y., Wong, L., Gao, G., Chen, S., Chen, Z., Ma, D., Bartlam, M., and Rao, Z. (2005) Design of Wide-Spectrum Inhibitors Targeting Coronavirus Main Proteases. *PLoS Biol. 3*, No. e324.

(6) Xue, X., Yu, H., Yang, H., Xue, F., Wu, Z., Shen, W., Li, J., Zhou, Z., Ding, Y., Zhao, Q., Zhang, X. C., Liao, M., Bartlam, M., and Rao, Z. (2008) Structures of Two Coronavirus Main Proteases: Implications for Substrate Binding and Antiviral Drug Design. *J. Virol. 82*, 2515−2527.

(7) Steuber, H., and Hilgenfeld, R. (2010) Recent Advances in Targeting Viral Proteases for the Discovery of Novel Antivirals. *Curr. Top. Med. Chem. 10*, 323−345.

(8) Hegyi, A., and Ziebuhr, J. (2002) Conservation of substrate specificities among coronavirus main proteases. *J. Gen. Virol. 83*, 595−599.

(9) Stadler, K., Masignani, V., Eickmann, M., Becker, S., Abrignani, S., Klenk, H.-D., and Rappuoli, R. (2003) SARS—beginning to understand a new virus. *Nat. Rev. Microbiol. 1*, 209−218.

(10) World Health Organization. Summary of probable SARS cases with onset of illness from 1 November 2002 to 31 July 2003. http://www.who.int/csr/sars/country/table2004_04_21/en/index.html (2004) (accessed on May 6, 2013).

(11) World Health Organization. Novel coronavirus infection in the United Kingdom. http://www.who.int/csr/don/2012_09_23/en/index.html (2012) (accessed on May 6, 2013).

(12) Zaki, A. M., Van Boheemen, S., Bestebroer, T. M., Osterhaus, A. D. M. E., and Fouchier, R. A. M. (2012) Isolation of a Novel Coronavirus from a Man with Pneumonia in Saudi Arabia. *N. Engl. J. Med. 367*, 1814−1820.

(13) Boheemen, S. van, Graaf, M. de, Lauber, C., Bestebroer, T. M., Raj, V. S., Zaki, A. M., Osterhaus, A. D. M. E., Haagmans, B. L., Gorbalenya, A. E., Snijder, E. J., and Fouchier, R. A. M. (2012) Genomic Characterization of a Newly Discovered Coronavirus Associated with Acute Respiratory Distress Syndrome in Humans. *MBio 3*, e00473−00412.

(14) World Health Organization. Novel coronavirus summary and literature update—as of 25 April 2013. http://www.who.int/csr/disease/coronavirus_infections/update_20130425/en/index.html (2013) (accessed on May 6, 2013).

(15) Solowiej, J., Thomson, J. A., Ryan, K., Luo, C., He, M., Lou, J., and Murray, B. W. (2008) Steady-state and pre-steady-state kinetic evaluation of severe acute respiratory syndrome coronavirus (SARS-CoV) 3CLpro cysteine protease: development of an ion-pair model for catalysis. *Biochemistry 47*, 2617−2630.

(16) Okamoto, D. N., Oliveira, L. C. G., Kondo, M. Y., Cezari, M. H. S., Szeltner, Z., Juhász, T., Juliano, M. A., Polgár, L., Juliano, L., and Gouvea, I. E. (2010) Increase of SARS-CoV 3CL peptidase activity due to macromolecular crowding effects in the milieu composition. *Biological Chemistry 391*, 1461−1468.

(17) Otto, H.-H., and Schirmeister, T. (1997) Cysteine Proteases and Their Inhibitors. *Chem. Rev. 97*, 133−172.

(18) Lewis, S. D., Johnson, F. A., and Shafer, J. A. (1976) Potentiometric determination of ionizations at the active site of papain. *Biochemistry 15*, 5009−5017.

(19) Creighton, D. J., Gessouroun, M. S., and Heapes, J. M. (1980) Is the thiolate—imidazolium ion pair the catalytically important form of papain? *FEBS Lett. 110*, 319−322.

(20) Johnson, F. A., Lewis, S. D., and Shafer, J. A. (1981) Determination of a low pK for histidine-159 in the S-methylthio derivative of papain by proton nuclear magnetic resonance spectroscopy. *Biochemistry 20*, 44−48.

(21) Lewis, S. D., Johnson, F. A., and Shafer, J. A. (1981) Effect of cysteine-25 on the ionization of histidine-159 in papain as determined by proton nuclear magnetic resonance spectroscopy. Evidence for a histidine-159-cysteine-25 ion pair and its possible role in catalysis. *Biochemistry 20*, 48−51.

(22) Harrison, M. J., Burton, N. A., and Hillier, I. H. (1997) Catalytic Mechanism of the Enzyme Papain: Predictions with a Hybrid Quantum Mechanical/Molecular Mechanical Potential. *J. Am. Chem. Soc. 119*, 12285−12291.

(23) Storer, A., and Ménard, R. (1994) Catalytic mechanism in papain family of cysteine peptidases, in *Methods in Enzymology* (Barrett, A. J., Ed.), pp 486−500, Academic Press, San Diego.

(24) Theodorou, L. G., Bieth, J. G., and Papamichael, E. M. (2007) The catalytic mode of cysteine proteinases of papain (C1) family. *Bioresour. Technol. 98*, 1931−1939.

(25) Shokhen, M., Khazanov, N., and Albeck, A. (2009) Challenging a paradigm: Theoretical calculations of the protonation state of the Cys25-His159 catalytic diad in free papain. *Proteins 77*, 916−926.

(26) Mladenovic, M., Fink, R. F., Thiel, W., Schirmeister, T., and Engels, B. (2008) On the Origin of the Stabilization of the Zwitterionic Resting State of Cysteine Proteases: A Theoretical Study. *J. Am. Chem. Soc. 130*, 8696−8705.

(27) Huang, C., Wei, P., Fan, K., Liu, Y., and Lai, L. (2004) 3C-like Proteinase from SARS Coronavirus Catalyzes Substrate Hydrolysis by a General Base Mechanism. *Biochemistry 43*, 4568−4574.

(28) Paasche, A., Schiller, M., Schirmeister, T., and Engels, B. (2010) Mechanistic Study of the Reaction of Thiol-Containing Enzymes with α,β-Unsaturated Carbonyl Substrates by Computation and Chemoassays. *ChemMedChem 5*, 869−880.

(29) Kalé, L., Skeel, R., Bhandarkar, M., Brunner, R., Gursoy, A., Krawetz, N., Phillips, J., Shinozaki, A., Varadarajan, K., and Schulten, K. (1999) NAMD2: Greater Scalability for Parallel Molecular Dynamics. *J. Comput. Phys. 151*, 283−312.

(30) Phillips, J. C., Braun, R., Wang, W., Gumbart, J., Tajkhorshid, E., Villa, E., Chipot, C., Skeel, R. D., Kalé, L., and Schulten, K. (2005) Scalable molecular dynamics with NAMD. *J. Comput. Chem. 26*, 1781−1802.

(31) Verlet, L. (1967) Computer "Experiments" on Classical Fluids. I. Thermodynamical Properties of Lennard-Jones Molecules. *Phys. Rev. 159*, 98−103.

(32) Andersen, H. C. (1983) Rattle: A "velocity" version of the shake algorithm for molecular dynamics calculations. *J. Comput. Phys. 52*, 24−34.

(33) WangH.KimY.T.MuramatsuT.TakemotoC.ShirouzuM.YokoyamaS.Crystal structure of SARS coronavirus main proteinase (3CLPRO), Protein Data Bank 2DUC, 2007, DOI: 10.2210/pdb2duc/pdb .

(34) Berman, H. M., Westbrook, J., Feng, Z., Gilliland, G., Bhat, T. N., Weissig, H., Shindyalov, I. N., and Bourne, P. E. (2000) The Protein Data Bank. *Nucleic Acids Res. 28*, 235−242.

(35) Bas, D. C., Rogers, D. M., and Jensen, J. H. (2008) Very fast prediction and rationalization of pKa values for protein-ligand complexes. *Proteins 73*, 765−783.
(36) Olsson, M. H. M., Søndergaard, C. R., Rostkowski, M., and Jensen, J. H. (2011) PROPKA3: Consistent Treatment of Internal and Surface Residues in Empirical pKa Predictions. *J. Am. Chem. Soc. 7*, 525−537.
(37) Rostkowski, M., Olsson, M., Sondergaard, C., and Jensen, J. (2011) Graphical analysis of pH-dependent properties of proteins predicted using PROPKA. *BMC Struct. Biol. 11*, 6.
(38) Jorgensen, W. L., Chandrasekhar, J., Madura, J. D., Impey, R. W., and Klein, M. L. (1983) Comparison of simple potential functions for simulating liquid water. *J. Chem. Phys. 79*, 926−935.
(39) Humphrey, W., Dalke, A., and Schulten, K. (1996) VMD: visual molecular dynamics. *J. Mol. Graph. 14* (33−38), 27−28.
(40) Sherwood, P., De Vries, A. H., Guest, M. F., Schreckenbach, G., Catlow, C. R. A., French, S. A., Sokol, A. A., Bromley, S. T., Thiel, W., Turner, A. J., Billeter, S., Terstegen, F., Thiel, S., Kendrick, J., Rogers, S. C., Casci, J., Watson, M., King, F., Karlsen, E., Sjøvoll, M., Fahmi, A., Schäfer, A., and Lennartz, C. (2003) QUASI: A general purpose implementation of the QM/MM approach and its application to problems in catalysis. *J. Mol. Struct. 632*, 1−28.
(41) Ahlrichs, R., Bär, M., Häser, M., Horn, H., and Kölmel, C. (1989) Electronic structure calculations on workstation computers: The program system turbomole. *Chem. Phys. Lett. 162*, 165−169.
(42) Engels, B., and Peyerimhoff, S. D. (1989) Theoretical study of FC2H4. *J. Phys. Chem. 93*, 4462−4470.
(43) Perić, M., Engels, B., and Peyerimhoff, S. D. (1991) Ab initio investigation of the vibronic structure of the C2H spectrum: Calculation of the hyperfine coupling constants for the three lowest-lying electronic states. *J. Mol. Spectrosc. 150*, 56−69.
(44) Paasche, A., Schirmeister, T., and Engels, B. (2013) Benchmark Study for the Cysteine−Histidine Proton Transfer Reaction in a Protein Environment: Gas Phase, COSMO, QM/MM Approaches. *J. Chem. Theory Comput. 9*, 1765−1777.
(45) Becke, A. D. (1993) A new mixing of Hartree−Fock and local density-functional theories. *J. Chem. Phys. 98*, 1372.
(46) Becke, A. D. (1993) Density-functional thermochemistry. III. The role of exact exchange. *J. Chem. Phys. 98*, 5648.
(47) Lee, C., Yang, W., and Parr, R. G. (1988) Development of the Colle-Salvetti correlation-energy formula into a functional of the electron density. *Phys. Rev. B 37*, 785.
(48) Schäfer, A., Horn, H., and Ahlrichs, R. (1992) Fully optimized contracted Gaussian basis sets for atoms Li to Kr. *J. Chem. Phys. 97*, 2571−2577.
(49) Weigend, F., and Ahlrichs, R. (2005) Balanced basis sets of split valence, triple zeta valence and quadruple zeta valence quality for H to Rn: Design and assessment of accuracy. *Phys. Chem. Chem. Phys. 7*, 3297.
(50) Eichkorn, K., Weigend, F., Treutler, O., and Ahlrichs, R. (1997) Auxiliary basis sets for main row atoms and transition metals and their use to approximate Coulomb potentials. *Theor. Chem. Acc. 97*, 119−124.
(51) Kendall, R. A., and Früchtl, H. A. (1997) The impact of the resolution of the identity approximate integral method on modern ab initio algorithm development. *Theor. Chem. Acc. 97*, 158−163.
(52) Schäfer, A., Huber, C., and Ahlrichs, R. (1994) Fully optimized contracted Gaussian basis sets of triple zeta valence quality for atoms Li to Kr. *J. Chem. Phys. 100*, 5829.
(53) Weigend, F. (2006) Accurate Coulomb-fitting basis sets for H to Rn. *Phys. Chem. Chem. Phys. 8*, 1057−1065.
(54) Paasche, A., Arnone, M., Fink, R. F., Schirmeister, T., and Engels, B. (2009) Origin of the Reactivity Differences of Substituted Aziridines: CN vs CC Bond Breakages. *J. Org. Chem. 74*, 5244−5249.
(55) Mladenovic, M., Junold, K., Fink, R. F., Thiel, W., Schirmeister, T., and Engels, B. (2008) Atomistic Insights into the Inhibition of Cysteine Proteases: First QM/MM Calculations Clarifying the Regiospecificity and the Inhibition Potency of Epoxide- and Aziridine-Based Inhibitors. *J. Phys. Chem. B 112*, 5458−5469.
(56) Mladenovic, M., Schirmeister, T., Thiel, S., Thiel, W., and Engels, B. (2007) The Importance of the Active Site Histidine for the Activity of Epoxide- or Aziridine-Based Inhibitors of Cysteine Proteases. *ChemMedChem 2*, 120−128.
(57) Buback, V., Mladenovic, M., Engels, B., and Schirmeister, T. (2009) Rational Design of Improved Aziridine-Based Inhibitors of Cysteine Proteases. *J. Phys. Chem. B 113*, 5282−5289.
(58) MacKerell, Bashford, D., Bellott, Dunbrack, Evanseck, J. D., Field, M. J., Fischer, S., Gao, J., Guo, H., Ha, S., Joseph-McCarthy, D., Kuchnir, L., Kuczera, K., Lau, F. T. K., Mattos, C., Michnick, S., Ngo, T., Nguyen, D. T., Prodhom, B., Reiher, W. E., Roux, B., Schlenkrich, M., Smith, J. C., Stote, R., Straub, J., Watanabe, M., Wiórkiewicz-Kuczera, J., Yin, D., and Karplus, M. (1998) All-Atom Empirical Potential for Molecular Modeling and Dynamics Studies of Proteins. *J. Phys. Chem. B 102*, 3586−3616.
(59) Sinclair, P. E., De Vries, A., Sherwood, P., Richard A. Catlow, C., and Van Santen, R. A. (1998) Quantum-chemical studies of alkene chemisorption in chabazite: A comparison of cluster and embedded-cluster models. *J. Chem. Soc., Faraday Trans. 94*, 3401−3408.
(60) Field, M. J., Bash, P. A., and Karplus, M. (1990) A combined quantum mechanical and molecular mechanical potential for molecular dynamics simulations. *J. Comput. Chem. 11*, 700−733.
(61) Senn, H. M., and Thiel, W. (2009) QM/MM Methods for Biomolecular Systems. *Angew. Chem., Int. Ed. 48*, 1198−1229.
(62) Zhang, R., Lev, B., Cuervo, J. E., Noskov, S. Y., and Salahub, D. R. (2010) A Guide to QM/MM Methodology and Applications, *Advances in Quantum Chemistry*, pp 353−400, Elsevier, Amsterdam.
(63) Schmidt, T. C., Paasche, A., Grebner, C., Ansorg, K., Becker, J., Lee, W., and Engels, B. (2012) QM/MM Investigations Of Organic Chemistry Oriented Questions, *Topics in Current Chemistry*, pp 1−77, Springer, Berlin/Heidelberg.
(64) Billeter, S. R., Turner, A. J., and Thiel, W. (2000) Linear scaling geometry optimization and transition state search in hybrid delocalised internal coordinates. *Phys. Chem. Chem. Phys. 2*, 2177−2186.
(65) Bash, P. A., Field, M. J., Davenport, R. C., Petsko, G. A., Ringe, D., and Karplus, M. (1991) Computer simulation and analysis of the reaction pathway of triosephosphate isomerase. *Biochemistry 30*, 5826−5832.
(66) Mulholland, A. J., and Richards, W. G. (1997) Acetyl-CoA enolization in citrate synthase: A quantum mechanical/molecular mechanical (QM/MM) study. *Proteins 27*, 9−25.
(67) Wong, K. F., Watney, J. B., and Hammes-Schiffer, S. (2004) Analysis of Electrostatics and Correlated Motions for Hydride Transfer in Dihydrofolate Reductase. *J. Phys. Chem. B 108*, 12231−12241.
(68) Hensen, C., Hermann, J. C., Nam, K., Ma, S., Gao, J., and Höltje, H.-D. (2004) A Combined QM/MM Approach to Protein−Ligand Interactions: Polarization Effects of the HIV-1 Protease on Selected High Affinity Inhibitors. *J. Med. Chem. 47*, 6673−6680.
(69) Hermann, J. C., Hensen, C., Ridder, L., Mulholland, A. J., and Höltje, H.-D. (2005) Mechanisms of Antibiotic Resistance: QM/MM Modeling of the Acylation Reaction of a Class A β-Lactamase with Benzylpenicillin. *J. Am. Chem. Soc. 127*, 4454−4465.
(70) Kästner, J., and Sherwood, P. (2010) The ribosome catalyzes peptide bond formation by providing high ionic strength. *Mol. Phys. 108*, 293.
(71) Kamerlin, S. C. L., and Warshel, A. (2010) At the dawn of the 21st century: Is dynamics the missing link for understanding enzyme catalysis? *Proteins 78*, 1339−1375.
(72) Senn, H. M., Kästner, J., Breidung, J., and Thiel, W. (2009) Finite-temperature effects in enzymatic reactions—Insights from QM/MM free-energy simulations. *Can. J. Chem. 87*, 1322−1337.
(73) Klähn, M., Braun-Sand, S., Rosta, E., and Warshel, A. (2005) On Possible Pitfalls in ab Initio Quantum Mechanics/Molecular Mechanics Minimization Approaches for Studies of Enzymatic Reactions. *J. Phys. Chem. B 109*, 15645−15650.
(74) Sharma, R., Thorley, M., McNamara, J. P., Watt, C. I. F., and Burton, N. A. (2008) A computational study of the intramolecular deprotonation of a carbon acid in aqueous solution. *Phys. Chem. Chem. Phys. 10*, 2475.

(75) Grebner, C., Kästner, J., Thiel, W., and Engels, B. (2013) A New Tabu-Search-Based Algorithm for Solvation of Proteins. *J. Chem. Theory Comput. 9*, 814−821.
(76) Walker, R. C., Crowley, M. F., and Case, D. A. (2008) The implementation of a fast and accurate QM/MM potential method in Amber. *J. Comput. Chem. 29*, 1019−1031.
(77) Case, D. A., Darden, T. A., Cheatham, T. E., III, Simmerling, C. L., Wang, J., Duke, R. E., Luo, R., Walker, R. C., Zhang, W., Merz, K. M., Roberts, B., Wang, B., Hayik, S., Roitberg, A., Seabra, G., Kolossvai, I., Wong, K. F., Paesani, F., Vanicek, J., Liu, J., Wu, X., Brozell, S. R., Steinbrecher, T., Gohlke, H., Cai, Q., Ye, X., Wang, J., Hsieh, M.-J., Cui, G., Roe, D. R., Mathews, D. H., Seetin, M. G., Sagui, C., Babin, V., Luchko, T., Gusarov, S., Kovalenko, A., and P. A. Kollman (2010) *AMBER 11*, University of California, San Francisco.
(78) Stewart, J. J. P. (1989) Optimization of parameters for semiempirical methods I. Method. *J. Comput. Chem. 10*, 209−220.
(79) Repasky, M. P., Chandrasekhar, J., and Jorgensen, W. L. (2002) PDDG/PM3 and PDDG/MNDO. Improved semiempirical methods. *J. Comput. Chem. 23*, 1601−1622.
(80) Hornak, V., Abel, R., Okur, A., Strockbine, B., Roitberg, A., and Simmerling, C. (2006) Comparison of multiple Amber force fields and development of improved protein backbone parameters. *Proteins 65*, 712−725.
(81) Torrie, G. M., and Valleau, J. P. (1977) Nonphysical sampling distributions in Monte Carlo free-energy estimation: Umbrella sampling. *J. Comput. Phys. 23*, 187−199.
(82) Souaille, M., and Roux, B. (2001) Extension to the weighted histogram analysis method: combining umbrella sampling with free energy calculations. *Comput. Phys. Commun. 135*, 40−57.
(83) Tissot, A. C., Vuilleumier, S., and Fersht, A. R. (1996) Importance of Two Buried Salt Bridges in the Stability and Folding Pathway of Barnase. *Biochemistry 35*, 6786−6794.
(84) Zheng, K., Ma, G., Zhou, J., Zen, M., Zhao, W., Jiang, Y., Yu, Q., and Feng, J. (2007) Insight into the activity of SARS main protease: Molecular dynamics study of dimeric and monomeric form of enzyme. *Proteins 66*, 467−479.
(85) Chen, S., Hu, T., Zhang, J., Chen, J., Chen, K., Ding, J., Jiang, H., and Shen, X. (2008) Mutation of Gly-11 on the dimer interface results in the complete crystallographic dimer dissociation of severe acute respiratory syndrome coronavirus 3C-like protease: crystal structure with molecular dynamics simulations. *J. Biol. Chem. 283*, 554−564.
(86) Shi, J., Sivaraman, J., and Song, J. (2008) Mechanism for Controlling the Dimer-Monomer Switch and Coupling Dimerization to Catalysis of the Severe Acute Respiratory Syndrome Coronavirus 3C-Like Protease. *J. Virol. 82*, 4620−4629.
(87) Fan, K., Wei, P., Feng, Q., Chen, S., Huang, C., Ma, L., Lai, B., Pei, J., Liu, Y., Chen, J., and Lai, L. (2004) Biosynthesis, Purification, and Substrate Specificity of Severe Acute Respiratory Syndrome Coronavirus 3C-like Proteinase. *J. Biol. Chem. 279*, 1637−1642.
(88) Chen, H., Wei, P., Huang, C., Tan, L., Liu, Y., and Lai, L. (2006) Only One Protomer Is Active in the Dimer of SARS 3C-like Proteinase. *J. Biol. Chem. 281*, 13894−13898.
(89) Derat, E., Shaik, S., Rovira, C., Vidossich, P., and Alfonso-Prieto, M. (2007) The Effect of a Water Molecule on the Mechanism of Formation of Compound 0 in Horseradish Peroxidase. *J. Am. Chem. Soc. 129*, 6346−6347.
(90) Kaukonen, M., Söderhjelm, P., Heimdal, J., and Ryde, U. (2008) Proton Transfer at Metal Sites in Proteins Studied by Quantum Mechanical Free-Energy Perturbations. *J. Chem. Theory Comput. 4*, 985−1001.
(91) Lee, W., Luckner, S. R., Kisker, C., Tonge, P. J., and Engels, B. (2011) Elucidation of the Protonation States of the Catalytic Residues in mtKasA: Implications for Inhibitor Design. *Biochemistry 50*, 5743−5756.
(92) Cheng, Y., Cheng, X., Radić, Z., and McCammon, J. A. (2007) Acetylcholinesterase: Mechanisms of Covalent Inhibition of Wild-Type and H447I Mutant Determined by Computational Analyses. *J. Am. Chem. Soc. 129*, 6562−6570.
(93) Tachikawa, H., Igarashi, M., Nishihira, J., and Ishibashi, T. (2005) Ab initio model study on acetylcholinesterase catalysis: potential energy surfaces of the proton transfer reactions. *J. Photochem. Photobiol., B 79*, 11−23.
(94) Lu, I.-L., Mahindroo, N., Liang, P.-H., Peng, Y.-H., Kuo, C.-J., Tsai, K.-C., Hsieh, H.-P., Chao, Y.-S., and Wu, S.-Y. (2006) Structure-Based Drug Design and Structural Biology Study of Novel Nonpeptide Inhibitors of Severe Acute Respiratory Syndrome Coronavirus Main Protease. *J. Med. Chem. 49*, 5154−5161.
(95) Lee, T.-W., Cherney, M. M., Liu, J., James, K. E., Powers, J. C., Eltis, L. D., and James, M. N. G. (2007) Crystal structures reveal an induced-fit binding of a substrate-like Aza-peptide epoxide to SARS coronavirus main peptidase. *J. Mol. Biol. 366*, 916−932.
(96) Xue, X., Yang, H., Shen, W., Zhao, Q., Li, J., Yang, K., Chen, C., Jin, Y., Bartlam, M., and Rao, Z. (2007) Production of Authentic SARS-CoV Mpro with Enhanced Activity: Application as a Novel Tag-cleavage Endopeptidase for Protein Overproduction. *J. Mol. Biol. 366*, 965−975.
(97) Yin, J., Niu, C., Cherney, M. M., Zhang, J., Huitema, C., Eltis, L. D., Vederas, J. C., and James, M. N. G. (2007) A Mechanistic View of Enzyme Inhibition and Peptide Hydrolysis in the Active Site of the SARS-CoV 3C-like Peptidase. *J. Mol. Biol. 371*, 1060−1074.
(98) Yang, S., Chen, S.-J., Hsu, M.-F., Wu, J.-D., Tseng, C.-T. K., Liu, Y.-F., Chen, H.-C., Kuo, C.-W., Wu, C.-S., Chang, L.-W., Chen, W.-C., Liao, S.-Y., Chang, T.-Y., Hung, H.-H., Shr, H.-L., Liu, C.-Y., Huang, Y.-A., Chang, L.-Y., Hsu, J.-C., Peters, C. J., Wang, A. H.-J., and Hsu, M.-C. (2006) Synthesis, crystal structure, structure-activity relationships, and antiviral activity of a potent SARS coronavirus 3CL protease inhibitor. *J. Med. Chem. 49*, 4971−4980.
(99) Verschueren, K. H. G., Pumpor, K., Anemüller, S., Chen, S., Mesters, J. R., and Hilgenfeld, R. (2008) A structural view of the inactivation of the SARS coronavirus main proteinase by benzotriazole esters. *Chem. Biol. 15*, 597−606.
(100) Chuck, C.-P., Chen, C., Ke, Z., Chi-Cheong Wan, D., Chow, H.-F., and Wong, K.-B. (2013) Design, synthesis and crystallographic analysis of nitrile-based broad-spectrum peptidomimetic inhibitors for coronavirus 3C-like proteases. *Eur. J. Med. Chem. 59*, 1−6.
(101) Ghosh, A. K., Xi, K., Ratia, K., Santarsiero, B. D., Fu, W., Harcourt, B. H., Rota, P. A., Baker, S. C., Johnson, M. E., and Mesecar, A. D. (2005) Design and Synthesis of Peptidomimetic Severe Acute Respiratory Syndrome Chymotrypsin-like Protease Inhibitors. *J. Med. Chem. 48*, 6767−6771.
(102) Lee, T.-W., Cherney, M. M., Huitema, C., Liu, J., James, K. E., Powers, J. C., Eltis, L. D., and James, M. N. G. (2005) Crystal Structures of the Main Peptidase from the SARS Coronavirus Inhibited by a Substrate-like Aza-peptide Epoxide. *J. Mol. Biol. 353*, 1137−1151.
(103) Goetz, D. H., Choe, Y., Hansell, E., Chen, Y. T., McDowell, M., Jonsson, C. B., Roush, W. R., McKerrow, J., and Craik, C. S. (2007) Substrate Specificity Profiling and Identification of a New Class of Inhibitor for the Major Protease of the SARS Coronavirus. *Biochemistry 46*, 8744−8752.
(104) Akaji, K., Konno, H., Mitsui, H., Teruya, K., Shimamoto, Y., Hattori, Y., Ozaki, T., Kusunoki, M., and Sanjoh, A. (2011) Structure-Based Design, Synthesis, and Evaluation of Peptide-Mimetic SARS 3CL Protease Inhibitors. *J. Med. Chem. 54*, 7962−7973.
(105) Zhu, L., George, S., Schmidt, M. F., Al-Gharabli, S. I., Rademann, J., and Hilgenfeld, R. (2011) Peptide aldehyde inhibitors challenge the substrate specificity of the SARS-coronavirus main protease. *Antiviral Res. 92*, 204−212.
(106) Fan, K., Ma, L., Han, X., Liang, H., Wei, P., Liu, Y., and Lai, L. (2005) The substrate specificity of SARS coronavirus 3C-like proteinase. *Biochem. Biophys. Res. Commun. 329*, 934−940.
(107) Ma, J. C., and Dougherty, D. A. (1997) The Cation-Pi Interaction. *Chem. Rev. 97*, 1303−1324.
(108) Loewenthal, R., Sancho, J., and Fersht, A. R. (1992) Histidine-aromatic interactions in barnase: Elevation of histidine pKa and contribution to protein stability. *J. Mol. Biol. 224*, 759−770.
(109) Cauët, E., Rooman, M., Wintjens, R., Liévin, J., and Biot, C. (2005) Histidine−Aromatic Interactions in Proteins and Protein−Ligand Complexes: Quantum Chemical Study of X-ray and Model Structures. *J. Chem. Theory Comput. 1*, 472−483.

(110) Pang, Y.-P. (2004) Three-dimensional model of a substrate-bound SARS chymotrypsin-like cysteine proteinase predicted by multiple molecular dynamics simulations: catalytic efficiency regulated by substrate binding. *Proteins 57*, 747−757.
(111) Zhong, D., Pal, S. K., and Zewail, A. H. (2011) Biological water: A critique. *Chem. Phys. Lett. 503*, 1−11.
(112) Pal, S. K., Peon, J., and Zewail, A. H. (2002) Biological water at the protein surface: Dynamical solvation probed directly with femtosecond resolution. *Proc. Natl. Acad. Sci. U.S.A. 99*, 1763−1768.
(113) Nandi, N., and Bagchi, B. (1997) Dielectric Relaxation of Biological Water. *J. Phys. Chem. B 101*, 10954−10961.
(114) Christ, C. D., Mark, A. E., and Van Gunsteren, W. F. (2010) Basic ingredients of free energy calculations: A review. *J. Comput. Chem. 31*, 1569−1582.
(115) Jorgensen, W. L. (1989) Free energy calculations: a breakthrough for modeling organic chemistry in solution. *Acc. Chem. Res. 22*, 184−189.
(116) Roux, B. (1995) The calculation of the potential of mean force using computer simulations. *Comput. Phys. Commun. 91*, 275−282.
(117) Hu, H., and Yang, W. (2009) Development and application of ab initio QM/MM methods for mechanistic simulation of reactions in solution and in enzymes. *J. Mol. Struct.: THEOCHEM 898*, 17−30.
(118) Hu, H., and Yang, W. (2008) Free Energies of Chemical Reactions in Solution and in Enzymes with Ab Initio Quantum Mechanics/Molecular Mechanics Methods. *Annu. Rev. Phys. Chem. 59*, 573−601.
(119) Zhang, Y., Liu, H., and Yang, W. (2000) Free energy calculation on enzyme reactions with an efficient iterative procedure to determine minimum energy paths on a combined ab initio QM/MM potential energy surface. *J. Chem. Phys. 112*, 3483−3492.
(120) Kaukonen, M., Söderhjelm, P., Heimdal, J., and Ryde, U. (2008) QM/MM−PBSA Method To Estimate Free Energies for Reactions in Proteins. *J. Phys. Chem. B 112*, 12537−12548.
(121) Marx, D. (2006) Proton Transfer 200 Years after von Grotthuss: Insights from Ab Initio Simulations. *ChemPhysChem 7*, 1848−1870.
(122) Marx, D. (2007) Proton Transfer 200 Years after von Grotthuss: Insights from Ab Initio Simulations. *ChemPhysChem 8*, 209−210.
(123) Bhattacharyya, K. (2003) Solvation Dynamics and Proton Transfer in Supramolecular Assemblies. *Acc. Chem. Res. 36*, 95−101.
(124) Carpino, L. A. (1993) 1-Hydroxy-7-azabenzotriazole. An efficient peptide coupling additive. *J. Am. Chem. Soc. 115*, 4397−4398.
(125) Grossman, M., Born, B., Heyden, M., Tworowski, D., Fields, G. B., Sagi, I., and Havenith, M. (2011) Correlated structural kinetics and retarded solvent dynamics at the metalloprotease active site. *Nat. Struct. Mol. Biol. 18*, 1102−1108.
(126) Chaplin, M. (2006) Do we underestimate the importance of water in cell biology? *Nat. Rev. Mol. Cell Biol. 7*, 861−866.
(127) Shie, J.-J., Fang, J.-M., Kuo, T.-H., Kuo, C.-J., Liang, P.-H., Huang, H.-J., Wu, Y.-T., Jan, J.-T., Cheng, Y.-S. E., and Wong, C.-H. (2005) Inhibition of the severe acute respiratory syndrome 3CL protease by peptidomimetic alpha,beta-unsaturated esters. *Bioorg. Med. Chem. 13*, 5240−5252.
(128) Kaeppler, U., Stiefl, N., Schiller, M., Vicik, R., Breuning, A., Schmitz, W., Rupprecht, D., Schmuck, C., Baumann, K., Ziebuhr, J., and Schirmeister, T. (2005) A new lead for nonpeptidic active-site-directed inhibitors of the severe acute respiratory syndrome coronavirus main protease discovered by a combination of screening and docking methods. *J. Med. Chem. 48*, 6832−6842.
(129) Martina, E., Stiefl, N., Degel, B., Schulz, F., Breuning, A., Schiller, M., Vicik, R., Baumann, K., Ziebuhr, J., and Schirmeister, T. (2005) Screening of electrophilic compounds yields an aziridinyl peptide as new active-site directed SARS-CoV main protease inhibitor. *Bioorg. Med. Chem. Lett. 15*, 5365−5369.
(130) Wu, C.-Y., King, K.-Y., Kuo, C.-J., Fang, J.-M., Wu, Y.-T., Ho, M.-Y., Liao, C.-L., Shie, J.-J., Liang, P.-H., and Wong, C.-H. (2006) Stable Benzotriazole Esters as Mechanism-Based Inactivators of the Severe Acute Respiratory Syndrome 3CL Protease. *Chem. Biol. 13*, 261−268.
(131) Akaji, K., Konno, H., Onozuka, M., Makino, A., Saito, H., and Nosaka, K. (2008) Evaluation of peptide-aldehyde inhibitors using R188I mutant of SARS 3CL protease as a proteolysis-resistant mutant. *Bioorg. Med. Chem. 16*, 9400−9408.